https://doi.org/10.5194/egusphere-2026-3708
Preprint. Discussion started: 10 July 2026

Species-explicit inventory of forest biogenic volatile organic emissions across China with MEGAN v3.2

Hao Liu[1], Hao Xu[2], Yixin Huang[1], Wei Zhou[3], Yunting Xiao[1], Qinghao Guo[1], Xi Zhao[1], Junjun Deng[1], Yele Sun[3], Pingqing Fu[1] & Jialei Zhu[1*]

[1] Institute of Surface-Earth System Science, School of Earth System Science, Tianjin University, Tianjin 300072, China.
[2] International Institute for Applied Systems Analysis, Schlossplatz 1, Laxenburg 2361, Austria.
[3] State Key Laboratory of Atmospheric Environment and Extreme Meteorology, Institute of Atmospheric Physics, Chinese Academy of Sciences, Beijing 100029, China.

Correspondence to: Jialei Zhu (zhujialei@tju.edu.cn)

https://doi.org/10.5194/egusphere-2026-3708
Preprint. Discussion started: 10 July 2026

Abstract.

Biogenic volatile organic compounds (BVOCs) are important precursors of secondary organic aerosols and tropospheric ozone, yet their emissions are commonly modelled at the plant functional type (PFT) level, which obscures substantial interspecies variability. This limitation is particularly acute for China, where high forest diversity and ambitious afforestation initiatives are expected to reshape national BVOC budgets. Here, we present a species-explicit BVOC emissions inventory for China covering 234 tree species (https://doi.org/10.5281/zenodo.20396128, Liu et al., 2026). The inventory was developed within the Model of Emissions of Gases and Aerosols from Nature (MEGAN) v3.2 modeling framework, with refined inputs comprising species-specific emission factors and high-resolution forest composition data for China. Total forest BVOC emissions were estimated at 10.26 Tg in 2019, with summer emissions accounting for about 50% of the annual total and a clear decreasing gradient from southern to northern China. Emissions were highly concentrated among a limited number of species: the five largest contributors, *Pinus massoniana*, *Quercus liaotungensis*, *Phyllostachys edulis*, *Cunninghamia lanceolata*, and *Quercus variabilis* accounted for 41.7% of total emissions while occupying only 25.4% of forest area. At the compound-class level, *Quercus liaotungensis* dominated isoprene emissions, whereas *Pinus massoniana* was the leading contributor to monoterpene emissions. Applying this species-explicit framework to two future afforestation scenarios with identical planted areas but contrasting species composition, we found that BVOC emissions may increase by 4.65 Tg yr^{-1} with the biomass-maximization tree species and by 5.10 Tg yr^{-1} under the most environmental-suitability species. The dominant compound class and species contributors differed markedly between scenarios, indicating that afforestation-driven BVOC responses depend strongly on species selection. These results demonstrate the importance of incorporating species-specific emission traits BVOC models and suggest that future afforestation strategies could substantially reshape both the magnitude and chemical composition of biogenic emissions, with implications for atmospheric chemistry and air quality.

1 Introduction

Biogenic volatile organic compounds (BVOCs) comprise ~90% of atmospheric non-methane organic vapors and contribute ~1000 Tg of reactive carbon to the troposphere annually (Goldstein et al., 2007; Guenther et al., 2012), with forests accounting for the dominant share (~90%) of global emissions. After being released by plants, BVOCs undergo rapid atmospheric oxidation and substantially influence the formation of secondary organic aerosol (SOA) and tropospheric ozone (Zhu et al., 2025; Xu et al., 2025). BVOC-derived SOA scatters solar radiation and nucleates clouds, altering precipitation (Pöschl et al., 2010), and accounts for 15-80% of atmospheric fine particulate matter responsible for regional haze (Kenseth et al., 2023), while tropospheric ozone acts as both a photochemical pollutant and greenhouse gas (Stenke et al., 2020). These processes establish BVOC emissions as a natural linkage governing the interplay between ecosystems, air quality (Rissanen et al., 2025), and climate (Sanaei et al., 2023). Accurate quantification of BVOC emissions is therefore essential for understanding ecosystem–atmosphere interactions and for informing climate mitigation and air quality improvement strategies.

BVOC emissions are regulated by interacting physiological and environmental processes (Bergman et al., 2025). These short-lived, highly reactive compounds, such as isoprene, monoterpenes, and sesquiterpenes, mediate interplant

https://doi.org/10.5194/egusphere-2026-3708
Preprint. Discussion started: 10 July 2026

communication while modulating stress responses (Yu et al., 2024), both critical to terrestrial ecosystem stability. Their biosynthesis depends on photosynthesis, which supplies carbon and energy substrates, while their release is mediated by stomatal conductance and other diffusion pathways (Niinemets et al., 2003; Zhang et al., 2025). These controls vary with intrinsic plant traits, including leaf age, species identity, and plant functional type, and respond strongly to environmental conditions such as light, temperature, humidity, atmospheric CO_2 concentration, and drought stress (Li et al., 2024). Emission rates increase non-linearly with light and temperature up to an optimum (~40°C), but decline under severe heat stress (Wang et al., 2024b). Elevated CO_2 tends to suppress isoprene emissions, partially offsetting the stimulatory influence of warming (Sahu et al., 2023). Drought further complicates emission responses: moderate water deficit may transiently enhance emissions by increasing leaf temperature, whereas prolonged or severe drought ultimately suppresses emissions through physiological stress (Wang et al., 2022).

Current approaches to quantifying BVOC fluxes generally integrate vegetation-specific emission factors with environmental response algorithms, driven by land-cover and meteorological datasets (Guenther et al., 2012; Wang et al., 2016a). The Model of Emissions of Gases and Aerosols from Nature (MEGAN) stands as the most widely adopted framework, incorporating canopy-scale parameterizations and environmental activity factors related to radiation, temperature, CO_2 concentration, phenology and soil moisture (Guenther et al., 2012). Using such frameworks, previous researches have quantified the effects of climate change, rising CO_2 drought and land-use change on BVOC emissions. For example, warming and enhanced radiation have increased global isoprene emissions by ~1% annually in recent decades (Opacka et al.,2021), whereas elevated CO_2 and drought have exerted suppressing effects (Wang et al., 2024a; Wang et al., 2022). Land-cover change has also altered global BVOC budgets, particularly through tropical deforestation associated reductions in isoprene emissions (Chen et al., 2018; Vella et al., 2025).

Despite these advances, a central uncertainty in BVOCs modeling lies in the coarse representation of vegetation diversity (Wu et al., 2024). Due to differences in their physiological structures, each tree species exhibits inherent variations in physiological processes and photosynthetic capacity, leading to distinct differences in the composition and emission rates of BVOCs. Most emission inventories, including applications of MEGAN in China, represent vegetation at the PFT level, such as deciduous broadleaf forest, evergreen coniferous forest. Due to the lack of local input data at the tree species level in China, it is still unable to differentiate emissions at the species level, leading to substantial uncertainty in BVOC emissions estimates for China (Guenther et al., 2012). This approach assumes similar emission characteristics within each PFT and therefore cannot capture substantial interspecific differences in BVOC composition and emission rates. Field measurements show that species within the same PFT may exhibit sharply contrasting emission profiles. For instant, within temperate deciduous broadleaf trees, *Lonicera maackii* emits predominantly isoprene at a mean rate of 9.17 μg gdw^{-1} h^{-1}, whereas *Acer truncatum* emits mainly monoterpenes (2.29 μg gdw^{-1} h^{-1}) with only marginal isoprene fluxes (0.05 μg gdw^{-1} h^{-1}, Jing et al., 2020), although both may be assigned a uniform isoprene-dominated profile of 12 μg gdw^{-1} h^{-1} under a PFT-based scheme. Similarly, among temperate evergreen needleleaf species, *Platycladus orientalis* is characterized by strong monoterpene emissions (27.18 μg gdw^{-1} h^{-1}) with minimal isoprene (1.60 μg gdw^{-1} h^{-1}), while *Taxus cuspidata* emits primarily isoprene (5.86 μg gdw^{-1} h^{-1}) with negligible monoterpenes (Jing et al., 2020). These discrepancies highlight PFT-based approaches may obscure species-level emission heterogeneity and contribute to substantial uncertainty in China's BVOC emission inventories.

This limitation is particularly consequential for China, where extensive forest cover, high tree diversity, and large-scale afforestation may substantially reshape national BVOC emissions. China's forests contain approximately 142.6

https://doi.org/10.5194/egusphere-2026-3708
Preprint. Discussion started: 10 July 2026

billion trees over 220 million hectares currently (based on Ninth National Forest Resource Inventory during 2009-2013) (SFGA, 2020; Cheng et al., 2025), equivalent to 23% of its national territory. Driven by complex topography and climatic heterogeneity, this vast territory sustains 4,886 distinct tree species (BGCI, 2021), of which 234 dominant species accounting for more than 90% forest area. This combination of extensive forest distribution, heterogeneous species composition, and strong climatic gradients make China an important but uncertain source of BVOCs (Cao et al., 2022). Meanwhile, China has committed to expanding forestation (including afforestation and reforestation) as part of its pathway toward carbon neutrality by 2060 (Mallapaty, 2020; SFGA, 2016). Previous studies suggest that forestation and climate warming have already contributed to persistent rises in BVOC emissions in China and may further enhance future emissions under warming scenarios (Li et al., 2021; Wang et al., 2021; Liu et al., 2019). However, because existing estimates rarely resolve emissions at the species level, it remains unclear which tree species dominate current BVOC budgets and how alternative forestation species selection strategies may alter the magnitude, spatial distribution, and chemical composition of future emissions.

Here, we developed a species-resolved BVOC emission inventory for 234 dominant tree species across China's forests (https://doi.org/10.5281/zenodo.20396128, Liu et al., 2026). By moving beyond PFT-level representation, we quantified current forest BVOC emissions, identified dominant emitting species and compound classes, and evaluated emission changes under two forestation scenarios with identical planting areas but contrasting species compositions: a biomass-maximization scenario (BIO) and an environmental-suitability (SUIT) scenario (Xu et al., 2023a). This framework allows us to disentangle the roles of species-specific emission capacity, forest distribution, and local climate in shaping national BVOC emissions, providing new insight into how afforestation choices may influence atmospheric chemistry and regional air quality.

2 Methods

2.1 MEGAN Model

The Model of Emissions of Gases and Aerosols from Nature (MEGAN) is a mechanistic modeling framework designed to estimate the net emission of gases and aerosols from terrestrial ecosystems to atmosphere. It uses simplified mechanistic algorithms to represent the major known biological and environmental controls on biogenic emissions (Guenther et al., 2012). In this study, we applied MEGAN v3.2 to develop emission inventories of existing forests and future forestation-driven forest expansion in China (Guenther et al., 2020).

MEGAN v3.2 consists of three major computational modules (https://doi.org/10.5281/zenodo.10526206, Guenther et al., 2024a). First, the preprocessor module reformats land-cover and meteorological data to generate environmental inputs for the simulation domain. Second, the emission factor processor module derives landscape-averaged emission factors and light-dependent fractions through hierarchical integrating vegetation information. This processor combines three complementary datasets (https://doi.org/10.5281/zenodo.10939297, Guenther et al., 2024b): (1) vegetation growth-form datasets describing the spatial distribution of trees, shrubs, grasses, and crops; (2) ecotype classifications characterizing all emitting plant species and their proportional contributions within each grid cell; and (3) species-level emission factor libraries constrained by observation. This hierarchical approach enables MEGAN v3.2 to capture emission factor variability associated with differences in species composition, including among regions assigned to the same plant functional type. Third, the emission rate estimator module integrates the preprocessed environmental fields and emission factor distributions to compute gridded biogenic emission fluxes at each time step.

https://doi.org/10.5194/egusphere-2026-3708
Preprint. Discussion started: 10 July 2026

In the model, BVOC emissions are formulated as:

$$Emission = EF \bullet EA \bullet \rho \quad (1)$$

where EF (mg m^{-2} h^{-1}; from the emission factor processor module) represents the emission factor under standard environmental conditions (temperature = 30 ℃, photosynthetically active radiation = 1000 μmol m^{-2} s^{-1}), characterizing the intrinsic emission capacity of vegetation. EA (from the emission rate estimator module) is a dimensionless emission activity factor that accounts for departures from standard conditions driven by meteorology and vegetation state. ρ represents the production and consumption within the canopy. The emission factor is aggregated to the grid-cell level using the fractional coverage of different vegetation species:

$$EF = \sum_{tree=1}^{a} EF_{tree} \bullet f_{tree} + EF_{shrub} \bullet f_{shrub} + EF_{grass} \bullet f_{grass} + EF_{crop} \bullet f_{crop} \quad (2)$$

where EF_{tree}, EF_{shrub}, EF_{grass}, and EF_{crop} denote the emission factors associated with different vegetation species, and f represents their fractional area coverage within each model grid cell. Besides, emission activity factors (EA) dynamically modulate the baseline emission potential in response to changing environmental conditions:

$$EA_i = C_{CE} \bullet LAI \bullet \gamma_{P,i} \gamma_{T,i} \gamma_{A,i} \gamma_{SM,i} \gamma_{C,i} \quad (3)$$

where LAI is the leaf area index (m^2 m^{-2}) and γ terms are dimensionless activity scalars that describe the sensitivity of BVOC emissions to environmental and physiological drivers. Specifically, γ_P accounts for the response to solar radiation, γ_T represents the temperature dependence of emissions, γ_A reflects the influence of leaf age, γ_{SM} captures soil moisture stress effects, and γ_C describes the response to atmospheric CO_2 concentration. The canopy environment coefficient (C_{CE}) is assigned a value that results in $\gamma = 1$ for the standard conditions and is dependent on the canopy environment model being used. The detail introduction to MEGAN v3.2 refers to Guenther et al (2020).

2.2 Enhanced local input for China

To better represent the spatial heterogeneity of BVOCs emission potentials across China's diverse forest ecosystems, we integrated tree species distribution data with the MEGAN framework. This enhancement was achieved through updates to four core components within the model (Fig. 1): dominant species-level forest distribution to characterize vegetation diversity (Sect. 2.2.1), a species-specific emission factor database to account for interspecific variability in emission potentials (Sect. 2.2.2), enhanced leaf area index (Sect. 2.2.3) and land cover (Sect. 2.2.4) datasets to better describe canopy structure and forest extent.

2.2.1 Current tree species distribution

Tree species distribution data were incorporated into Eq. (2) to determine the species composition within each model grid cell f_{tree}, specifying the number of species occurring at the grid scale. These data are derived from a 1:1,000,000 vector map of forest type distribution (http://www.doi.org/10.12041/geodata.43370179401687.ver1.db, Chen et al., 2020), based on the forest inventory conducted during 2013-2017 by the China Forest Vegetation Survey project of the Chinese Academy of Forestry Sciences, which provides one of the most comprehensive species-level forest distribution datasets currently available for China. With the previous national forest record dating back to 1997 (*Forest in China*; Wu, 1997), this dataset is considered suited for characterizing forest conditions in our study. The original data were resampled to 1 km resolution to provide a spatial representation of ecotypes that replaces the plant

https://doi.org/10.5194/egusphere-2026-3708
Preprint. Discussion started: 10 July 2026

functional type classification in MEGAN (Fig. 1). Following Forest Resource Report of China (SFGA, 2020), forests in this study are defined as stands with canopy closure ≥ 0.2, which inherently excludes sparse woodlands and shrublands failing to meet the thresholds. The dataset encompasses 234 dominant taxa, covering 187 million hectares and accounting for 90% of the national forested area (SFGA, 2020). Among them, 225 taxa were resolved at the species level and ranked by individual contribution, whereas the remaining nine were assigned to aggregated functional-type classes to account for rare or taxonomically unresolved groups.

The 225 species-level taxa span 113 genera, among which the five most species-rich genera are *Pinus* (19 species), *Quercus* (15 species), *Populus* (10 species), *Castanopsis* (9 species), and *Phyllostachys* (8 species). These genera belong to 47 families, with Pinaceae (42 species), Fagaceae (32 species), Poaceae (17 species), Rosaceae (12 species), and Salicaceae (12 species) being the five most extensively represented. In contrast, the standard MEGAN PFT scheme aggregates this taxonomic diversity into only eight PFTs: broadleaf evergreen tropical forest, broadleaf evergreen temperate forest, broadleaf deciduous tropical forest, broadleaf deciduous temperate forest, broadleaf deciduous boreal forest, needleleaf evergreen temperate forest, needleleaf evergreen boreal forest, and needleleaf deciduous boreal forest.

Species-specific forested areas were computed through a systematic disaggregation procedure applied to the vector map (Fig. 1). All polygons were first classified as either pure stands, in which a single species accounts for the entire polygon area, or mixed stands, containing two or more co-dominant species. For pure-stand polygons, the full area was assigned directly to the dominant species (e.g., *Quercus mongolica* forest). In mixed-stand polygons, the total area was disaggregated among constituent species in equal proportions, that each of the n species received $1/n$ of the polygon area (e.g., a *Quercus mongolica* - *Populus davidiana* mixed forest polygon was split evenly, allocating 50% of the area to each species). This equal-proportion assumption was applied across all mixed stands because species-level area ratios were not available at the grid scale. Following disaggregation, all records were aggregated by species name through a group-by summation to obtain each of the 234 dominant tree species area. After disaggregation, polygon-level records were aggregated by species name through a group-by summation to obtain each of the 234 dominant tree species area. Thus, the area attributed to a given species represents both its full area in pure stands and its proportional area in mixed stands where it occurs as a co-dominant species. This species-level forest distribution inventory provides a spatially explicit basis for representing BVOC emission heterogeneity across China and enables more detailed emission estimates than conventional PFT-based classifications.

2.2.2 Emission factor database

We constructed a species-specific emission factor database through a comprehensive literature survey of field measurements and observational studies (Table C4). This database provides the EF_{tree} parameter required in Eq. (2). Emission factors are calculated by normalizing BVOC emission rates with leaf area:

$$Emission\ Factor = K / MW / SLA \quad (4)$$

where K denotes the emission rate (μg gdw^{-1} h^{-1}), MW represents the molecular weight (g mol^{-1}), and SLA is the specific leaf area (cm^2 gdw^{-1}) obtained from the FloraVeg.EU database (www.floraveg.eu/; Chytrý et al., 2024), an online repository documenting biological traits, ecological indicator values, and distributional information for plant species.

K values for the 234 tree species were derived from a comprehensive review of 184 peer-reviewed studies,

https://doi.org/10.5194/egusphere-2026-3708
Preprint. Discussion started: 10 July 2026

supplemented by Appendix 12 of *Understandi*ng i-Treea – a suite of computer software tools published by the United States Forest Service for assessing and quantifying urban forest resources (Nowak, 2024), as well as the default emission factor library embedded in MEGAN v3.2. These empirical K values are obtained through measurements conducted using dynamic chamber or static enclosure approaches, in which emitted BVOCs were collected onto automatic sampler and subsequently analyzed by gas chromatography-mass spectrometry (GC/MS). The majority of measurements were made under standardized conditions (temperature = 30 °C, photosynthetically active radiation = 1000 μmol m^{-2} s^{-1}). When emission rates for certain species vary across multiple sources, we prioritized the most frequently reported value or calculated the arithmetic mean of all available data. For species lacking published emission measurements, we estimated emission factors through a principle of credibility based on classifications from the China Plant Science Data Center (www.plantplus.cn). This process involved assigning values from congeneric species within the same genus or moving to the family level when genus-level data were unavailable. This systematic prioritization ensured that the most representative and taxonomically relevant information was utilized for each species in the database.

2.2.3 Leaf area index

The preprocessor module quantifies the amount of foliage across the simulation domain, thereby providing the LAI inputs required in Eq. (3). We employed the MODIS global LAI product (MCD15A2H, https://doi.org/10.5067/MODIS/MCD15A2H.061, Myneni et al., 2021) which features a 500-meter spatial resolution and 8-day temporal resolution (Fig. 1). The 2019 LAI datasets were integrated into the MEGAN model to replace the default 2003 inputs. This enhancement ensures that the LAI data used in our simulations are both temporally relevant with tree species distribution and spatially representative of the study period.

2.2.4 Land cover type

In the preprocessor module, land cover data were processed to determine the fractional coverage of each plant growth form, including trees (f_{tree}), shrubs (f_{shrub}), grasses (f_{grass}), and crops (f_{crop}), as required in Eq. (2). In this study, land-cover inputs were updated using the MODIS Land Cover Type product at 500m resolution (MCD12Q1, https://doi.org/10.5067/MODIS/MCD12Q1.061, Friedl et al., 2022). Each MODIS land-cover class was mapped to one or more plant growth-form categories following the MEGAN default land-cover crosswalk of specified fractional contributions (Fig. 1). The five core forest classes (evergreen needleleaf, evergreen broadleaf, deciduous needleleaf, deciduous broadleaf, and mixed forest) were assigned entirely to tree cover. Woody savannas were apportioned as 60% tree, 20% grass, and 20% shrub cover, while savannas were split into 30% tree, 35% grass, and 35% shrub cover. Closed shrublands were assigned entirely to shrub cover, whereas open shrublands were comprised 60% shrub and 40% grass cover. Natural vegetation mosaics were distributed equally across all four growth forms at 25% each. The fractional cover of each plant growth form within a coarse grid cell was then calculated by aggregating the weighted contributions of all relevant MODIS land-cover classes. Specifically, tree cover received contributions from the five core forest classes, woody savannas, savannas, and natural vegetation mosaics; grass and shrub cover were each aggregated from woody savannas, savannas, grasslands or shrublands, and natural vegetation mosaics; and crop cover was derived from croplands and natural vegetation mosaics.

https://doi.org/10.5194/egusphere-2026-3708
Preprint. Discussion started: 10 July 2026

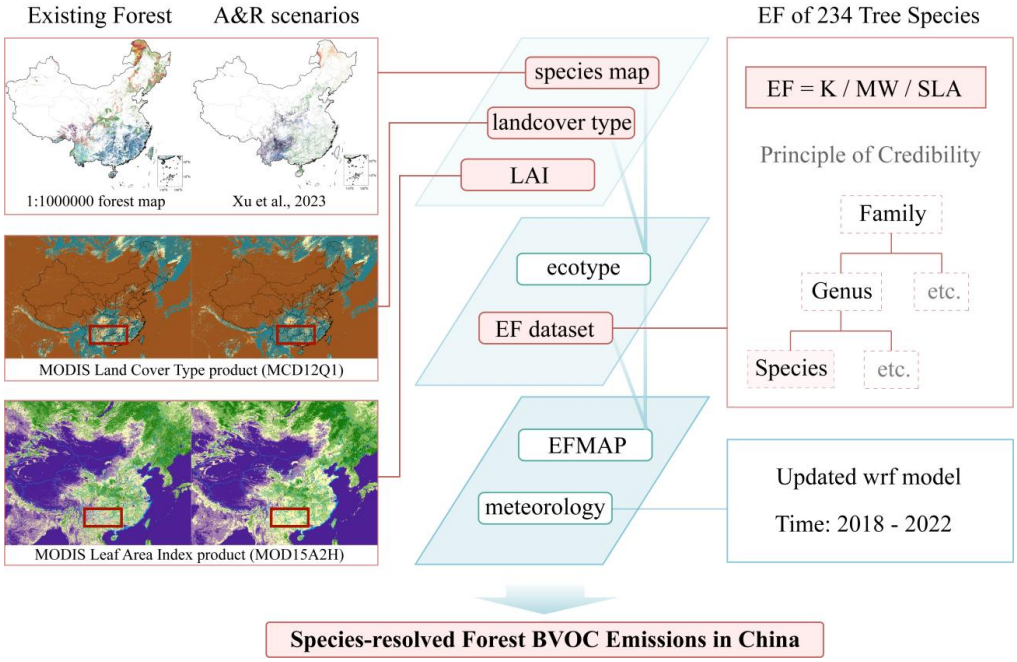

Figure 1 | Schematic overview of enhanced local inputs for estimating BVOC emissions in China from existing forests and afforestation & reforestation scenarios using the MEGAN model. Red boxes highlight the four key local input enhancements: (1) Species map: refined tree species distribution maps capturing China's vegetation diversity, Sect. 2.2.1; (2) EF dataset: a species-specific emission factor database accounting for inter-specific variability in emission potentials, Sect. 2.2.2; (3) LAI: an enhanced leaf area index dataset representing canopy structure, Sect. 2.2.3; and (4) Landcover type: revised land cover data, Sect. 2.2.4.

2.3 Implementation of afforestation & reforestation scenarios

To assess changes in BVOC emissions driven by future afforestation and reforestation (A&R) in China, we implemented two A&R scenarios from Xu et al. (2023a), with the dataset obtained from Zenodo (https://zenodo.org/records/8297679, Xu et al., 2023b). Both scenarios cover the same potential planting area of 78 Mha but differ in tree species selection strategies: a biomass-maximizing scenario (BIO) and a highest environmental suitability scenario (SUIT). To represent these scenarios in MEGAN, we updated three key surface inputs within the target A&R areas: forest cover fraction, tree species composition, and leaf area index (LAI). These inputs determine the tree growth-form fraction (f_{tree}) in Eq. (2) and the canopy foliage conditions required in Eq. (3).

2.3.1 Afforestation and reforestation scenarios

The BIO scenario prioritizes carbon sequestration through biomass-optimized tree species selection and was designed to achieve nearly twice the carbon storage of the SUIT scenario by the end of century. It is mainly composed of typical deciduous broadleaf forests (35.7%) in southeastern China and evergreen broadleaf forests (31.8%) in southwest China. The five most prevalent taxa in this scenario are *Cunninghamia lanceolata*, *Quercus aquifolioides*, *Camellia sinensis*, *Juglans* spp. and *Castanopsis delavayi*, with four being broadleaf species reflects their superior carbon storage capacity. Nevertheless, because species selection in BIO scenario is optimized primarily for biomass

https://doi.org/10.5194/egusphere-2026-3708
Preprint. Discussion started: 10 July 2026

accumulation, this scenario may not necessarily maximize other ecological benefits, such as biodiversity conservation, soil erosion control, or water provision.

In contrast, the SUIT scenario emphasizes ecological suitability of tree species to ensure long-term forest stability and climate adaptability. Species allocation in this scenario follows local climatic and ecological conditions to reduce the risk of plantation failure caused by water stress or species-environment mismatch. *Pinus massoniana* forests (9.40%) are predominantly allocated to southeastern China, while other deciduous broadleaf forests (16.8%) and warm Pinaceae forests (17.5%) are concentrated in southern regions, Betula-Populus (11.6%) demonstrate tolerance to diverse climatic conditions across the country. Compared with BIO, the SUIT scenario includes a larger share of needleleaf forests, with four of its five most prevalent species (*Pinus yunnanensis*, *Pinus massoniana*, *Pinus tabuliformis* and *Pinus armandii*) being conifers, while *Betula platyphylla* is the only broadleaf species among the top five.

2.3.2 Tree cover fraction adjustments

Under the baseline (BASE) land-cover condition, the 78 Mha area identified for potential A&R consists of multiple land cover types, predominantly savannas, grasslands, and shrublands. In the A&R scenarios, target grid cells are converted to forest, with the forest cover fraction (f_{tree}) set to 1 to estimate the upper bound of potential A&R effects, representing a fully closed canopy in plantations (Fig. 1). The fractional covers of shrubs (f_{shrub}), grasses (f_{grass}), and crops (f_{crop}) in Eq. (2) are all set to zero. This adjustment ensures that BVOC emissions within A&R cells are dominated by the selected tree species, while leaving surrounding regions unchanged to preserve a consistent regional background.

2.3.3 Species composition in A&R

While the A&R scenarios define 15 forestation forest type (dominant species or group), but these categories are still too coarse for species-resolved BVOC emission estimation in MEGAN. We therefore developed a nearest-neighbor spatial matching procedure to disaggregate the 15 forestation forest types into species-level compositions.

For each A&R grid cell, we first identified existing forest cells belonging to the same forest type in the 1:1,000,000 tree species vector map of China (Chen et al., 2020). Among these candidate cells, the geographically nearest existing forest cell was selected based on Euclidean distance. The underlying assumption is that nearby existing forest cells within the same forest type provides the closest ecologically analogous for species composition, because they have established under broadly comparable environmental conditions. The species composition of matched existing forest cell was transferred to the corresponding A&R grid cell. Through this procedure, the 15 coarse forest type were spatially disaggregated into 234 tree species at 1 km resolution, yielding afforestation vector maps for both BIO and SUIT scenarios, thereby providing the kilometer-scale, species-level inputs required for estimating subsequent BVOC emissions.

2.3.4 Prediction of leaf area index under A&R scenarios

Since LAI observations are unavailable for future potential A&R landscapes, we developed a set of random forest models to estimate monthly LAI distributions across A&R grid cells (Fig. 1). Twelve independent models were trained, one per calendar month, using historical monthly LAI data from 2003 to 2018. Despite the initial inclusion of

https://doi.org/10.5194/egusphere-2026-3708
Preprint. Discussion started: 10 July 2026

climate variables (temperature, precipitation, relative humidity, shortwave radiation, sunshine duration, and surface pressure) as candidate predictors, feature importance analysis revealed their contributions to be marginal. The final models therefore retained four dominant land surface predictors: Fraction of Green Vegetation Cover (https://doi.org/10.2909/7d726671-9647-4116-8dc3-cf7470a1a782, CLMS, 2020), MCD12Q1 land cover classifications (https://doi.org/10.5067/MODIS/MCD12Q1.061, Friedl et al., 2022), soil properties from the Harmonized World Soil Database (https://www.fao.org/soils-portal/data-hub/soil-maps-and-databases/harmonized-world-soil-database-v12/en/, Fischer et al., 2008), and the 1:1,000,000 vector map of forest type distribution (http://www.doi.org/10.12041/geodata.43370179401687.ver1.db, Chen et al., 2020). Since each model is trained on data from a single calendar month, seasonal variability in LAI is implicitly captured across the twelve models rather than driven by climate forcing within any individual model, rendering climate variables largely redundant. Model performance was assessed through independent temporal validation, with models trained on 2003-2018 data and evaluated against MCD15A2H LAI observations for the corresponding months in 2019. Across all grid cells, the models achieved monthly correlation coefficients of 0.62-0.76, root mean square errors (RMSE) of 15.5-17.3, and mean absolute errors (MAE) of 9.5-11.3 (Table C1). To predict LAI under the A&R scenarios, baseline surface attributes were replaced with A&R-specific parameters, including species composition derived from the nearest-neighbor matching procedure and the enhanced forest fraction associated with plantation establishment, thereby enabling monthly LAI predictions under the A&R scenarios. The resulting monthly mean LAI fields were incorporated into Eq. (3) as surface input parameters, collectively representing the effects of vegetation cover change and canopy density modification on BVOC emissions.

2.4 Simulation scenarios

For existing forests, three scenarios were designed to characterize current forest BVOC emissions (Table 1): Exist-SPE conducted a total species-level forest simulation spanning 2018-2022, with the resulting five-year mean emissions used to drive WRF-Chem simulations of BSOA (2018-2020) for inventory evaluation. Exist-PFT adopted the conventional PFT-level scheme for 2019, serving as a benchmark to assess the improvement achieved by updating emission calculations from the PFT level to the species level. Exist-IND generated a set of individual emission inventories for each of the 234 tree species in 2019, enabling identification of the dominant contributors to China's forest BVOC emissions.

For A&R scenarios, BIO-IND and SUIT-IND applied the same species-resolved framework as Exist-IND to 2019 (Table 1), replacing current forest cover, species composition, and LAI with those derived from two A&R scenarios described in Sect. 2.3, respectively. These two scenarios quantify national emission changes attributable to A&R activities and also enable identification of dominant BVOC-emitting tree species under each A&R scenario. In both scenarios, meteorological fields were held constant at present-day conditions, consistent with those applied in Exist-IND, isolating the influence of A&R-driven changes in forest cover and composition on BVOC emissions from potential climate feedbacks.

In this study, the Weather Research and Forecasting model coupled with Chemistry (WRF-Chem version 4.2; Skamarock et al., 2019) was used to simulate meteorological field to drive biogenic emission estimation by MEGAN and to simulate SOA for evaluation of the emission inventory. As an online coupled mesoscale modeling system, WRF-Chem simulates trace gases and aerosols simultaneously with meteorological fields within a unified computational framework. It supports a wide range of gas-phase chemical mechanisms and aerosol schemes of varying

https://doi.org/10.5194/egusphere-2026-3708
Preprint. Discussion started: 10 July 2026

complexity, and incorporates parameterizations for photolysis, dry and wet deposition, biogenic and anthropogenic emissions, and SOA formation. The model was employed in two configurations. The chemistry module was disabled to run the model in meteorology-only mode, thereby generating the 2018-2022 meteorological fields as input for MEGAN v3.2 biogenic emission estimation. The fully coupled WRF-Chem configuration was then used to simulate SOA over the period 2018-2020, with results compared against observations to evaluate the derived emission inventory. To improve the representation of surface conditions, the default land cover and LAI in both configurations were replaced with enhanced datasets, as described in Sect. 2.2.

Both configurations share same domain and physical parameterization schemes (configuration detailed in Table C2). The model domain encompasses China and surrounding regions at a horizontal resolution of 27 km, with 35 vertical layers extending from the surface to 100 hPa. Initial and lateral boundary conditions are derived from the National Centers for Environmental Prediction Final (FNL, https://doi.org/10.5065/D6M043C6, NCEP, 2000) Analysis data at 1° spatial resolution and 6-hourly temporal resolution. The physical parameterization schemes include the Morrison double-moment scheme for microphysics (Morrison et al., 2009), the Grell-3D ensemble scheme for cumulus convection (Grell et al., 2014), the Rapid Radiative Transfer Model for GCMs scheme for shortwave and longwave radiation (Iacono et al., 2008), the Mellor-Yamada Nakanishi and Niino Level 2.5 scheme for the planetary boundary layer (Nakanishi et al., 2006), and the Community Land Model version 4 for the land surface (Oleson et al., 2013). For the coupled simulation, gas-phase chemistry is represented by the Model for Ozone and Related chemical Tracers scheme (Emmons et al., 2010), and aerosol processes are treated using the Model for Simulating Aerosol Interactions and Chemistry with 4 sectional aerosol bins (Zaveri et al., 2008). Anthropogenic emissions are prescribed using the 2020 Multi-resolution Emission Inventory for China (MEIC) and the 2017 MIX inventory for regions outside China (http://meicmodel.org.cn/, Cheng et al., 2023), while biogenic emissions are calculated by MEGAN v3.2 with improved model inputs.

Table 1 Simulation Scenarios

Scenario	Land Cover	Period	Purpose
Exist-SPE	species-level forest	2018-2022	Evaluate BSOA against observations
Exist-PFT	PFT-level forest	2019	PFT-level BVOC emissions
Exist-IND	234 tree species	2019	Species-level BVOC attribution
BIO-IND	BIO species	2019	BVOC response to carbon-prioritized A&R
SUIT-IND	SUIT species	2019	BVOC response to ecology-optimized A&R

3 Model evaluations

3.1 Validation with BVOC observations

To evaluate the species-resolved BVOC emissions inventory, observed emission rates of isoprene and monoterpenes from four forest monitoring stations were compared (Fig. 2; Bai et al., 2026). The selected stations include Changbai Mountain (CBM, 42°24’N, 128°6’E; Bai et al., 2015), Linan (LA, 30°18’N, 119°34’E; Bai et al., 2016), Qianyanzhou (QYZ, 26°44’N, 115°04’E; Bai et al., 2017) and Danzhou (DZ, 19°32’N, 109°28’E; Bai et al., 2025), spanning a broad latitudinal gradient from temperate to tropical forest ecosystems across China. Along this

https://doi.org/10.5194/egusphere-2026-3708
Preprint. Discussion started: 10 July 2026

gradient, floristic composition varies considerably, with dominant tree species exhibiting divergent BVOC emission potentials that conventional PFT-based classifications fail to capture.

Simulations with two parallel MEGAN3 configurations were conducted, one applying the default PFT emission factors (Exist-PFT) and the other the species-resolved scheme (Exist-SPE). The resulting BVOC emission rates from both schemes were evaluated against observational records from different periods between 2011 and 2019. For each monitoring station, the two scenarios shared identical meteorological and LAI inputs, ensuring a consistent atmospheric and vegetation density background across both simulations. The species-resolved scheme yielded more accurate concentration magnitudes than Exist-PFT. For isoprene, mean bias (MB) decreased from 1.28 to 1.03 mg m^{-2} h^{-1} and root mean square error (RMSE) from 1.83 to 1.52 mg m^{-2} h^{-1}. For monoterpenes, MB declined from 0.25 to 0.21 mg m^{-2} h^{-1} and RMSE from 1.31 to 1.09 mg m^{-2} h^{-1}. These reductions in bias demonstrate that species-level refinement reduces errors introduced by PFT averaging without altering the temporal patterns.

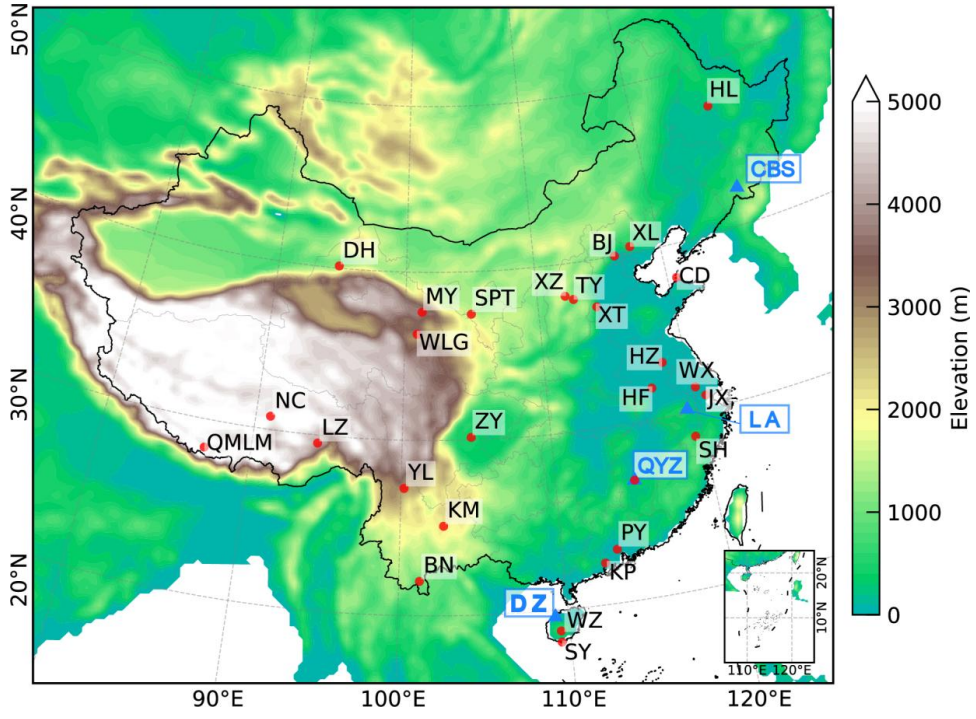

Figure 2 | Locations of BVOCs observation sites (CBS, LA, QYZ, and DZ; blue triangles) and 29 SOA observation sites (red circles) used for inventory evaluation. BVOC observations were used to evaluate simulated BVOC emissions, while SOA observations were used to assess model performance in reproducing secondary organic aerosol levels.

Site-specific analysis further highlighted the mechanistic benefits of the species-resolved scheme (Exist-SPE). The DZ station (Table C3), dominated by *Hevea brasiliensis*, was classified as tropical broadleaf forest in the PFT scheme, with emission factors of 8.59 nmol m^{-2} s^{-1} for isoprene and 0.61 nmol m^{-2} s^{-1} for monoterpenes. These values deviated from the measured values (isoprene: 0.09 nmol m^{-2} s^{-1}; monoterpenes: 2.22 nmol m^{-2} s^{-1}), leading to an overestimation of isoprene and underestimation of monoterpenes emission, with mean biases of +1.74 and -0.77 mg m^{-2} h^{-1}. In contrast, species-resolved scheme drew on field-measured emission factors, reduced isoprene mean bias to

https://doi.org/10.5194/egusphere-2026-3708
Preprint. Discussion started: 10 July 2026

+0.77 mg m^{-2} h^{-1} and monoterpene to -0.10 mg m^{-2} h^{-1}. These corrections brought both compounds into closer agreement with observations and reproduced the low isoprene but elevated monoterpene profile of tropical rubber plantations.

At QYZ station (Table C3), where *Pinus massoniana* dominates, the default PFT isoprene emission factor (8.30 nmol m^{-2} s^{-1}) exceeded the species-specific value (0.39 nmol m^{-2} s^{-1}) by more than an order of magnitude, leading to a systematic overestimation of emission (MB = 1.88, RMSE = 2.09 mg m^{-2} h^{-1}). Adopting the *Pinus massoniana* isoprene emission factor (0.39 nmol m^{-2} s^{-1}) reduced MB to 0.58 mg m^{-2} h^{-1} and RMSE to 0.68 mg m^{-2} h^{-1}. At LA station (Table C3), dominated by *Phyllostachys edulis*, the Exist-PFT also overestimated emissions (MB = 0.96, RMSE = 1.19 mg m^{-2} h^{-1}), while the species-specific factor reduced errors to MB = 0.39 and RMSE = 0.48 mg m^{-2} h^{-1}. At CBM station (Table C3), dominated by a mixture of *Betula platyphylla*, *Populus davidiana*, and *Quercus mongolica*, the species-resolved scheme reduced monoterpene bias (MB from 0.30 to 0.27 mg m^{-2} h^{-1}) but increased isoprene overestimation (MB from 0.27 to 0.71 mg m^{-2} h^{-1}), suggesting that uncertainty in species-specific emission factors for mixed temperate assemblages warrants further investigation.

Across all four sites, species-resolved scheme (Exist-SPE) eliminated the artificial smoothing inherent in PFT averaging, where a single value within same PFT conflates species whose emission factors differ by up to two orders of magnitude. The resulting BVOC emissions captured the flux ranges more faithfully than the Exist-PFT. The improvements in bias, error statistics, and temporal fidelity collectively confirm that species-specific emission factors elevate model performance, rendering the BVOC emissions inventory reliable for integration into regional atmospheric chemistry simulations, which is further supported by the BSOA evaluation in the following section.

3.2 Evaluation with SOA observations

To further validate the species-resolved BVOC emissions inventory (Exist-SPE), we integrated it into the Weather Research and Forecasting model coupled with Chemistry (WRF-Chem; configuration detailed in Table C2) to simulate BSOA over China during the period 2018-2020. The simulated BSOA concentrations were evaluated against ground-based observations from 29 monitoring stations across China (Fig. 2). This site-specific comparison revealed a strong correlation between simulated and observed values (correlation coefficient: r = 0.78). The mean simulated concentration across all stations was 3.01 μg m^{-3} (Fig. 3), compared to the observed mean of 4.37 μg m^{-3}, indicating a moderate systematic underestimation as reflected by the mean bias (MB = -1.36 μg m^{-3}). Error metrics further underscored the model's reliability, with a root mean square error (RMSE = 2.90 μg m^{-3}) and mean absolute error (MAE = 2.11 μg m^{-3}) demonstrating acceptable performance relative to the range of concentrations encountered (0.18-21.85 μg m^{-3}). The model underestimated concentrations at 24 out of the 29 stations, with performance varying systematically with observed concentration magnitude. At stations with low concentrations, the model exhibited close agreement, with mean bias below 1 μg m^{-3} at 10 stations, whereas large underestimations occurring at stations with high observed values (Fig. 3), such as CD (simulated: 2.00 μg m^{-3} vs. observed: 9.40 μg m^{-3}; difference: -7.40 μg m^{-3}), XT (2.45 vs. 8.80; -6.35 μg m^{-3}), and PY (7.47 vs. 12.50; -5.03 μg m^{-3}). These modeling biases reflect the combined effects of uncertainties in SOA formation pathways, incompletely resolved aerosol-phase processes, and anthropogenic emission inputs, which may compound under conditions of elevated precursor loading at high-concentration stations. Overall, the validation encompasses both aggregate statistics and site-level insights, providing robust evidence for the capability of the coupled modeling framework in simulating BSOA dynamics from biogenic sources.

https://doi.org/10.5194/egusphere-2026-3708
Preprint. Discussion started: 10 July 2026

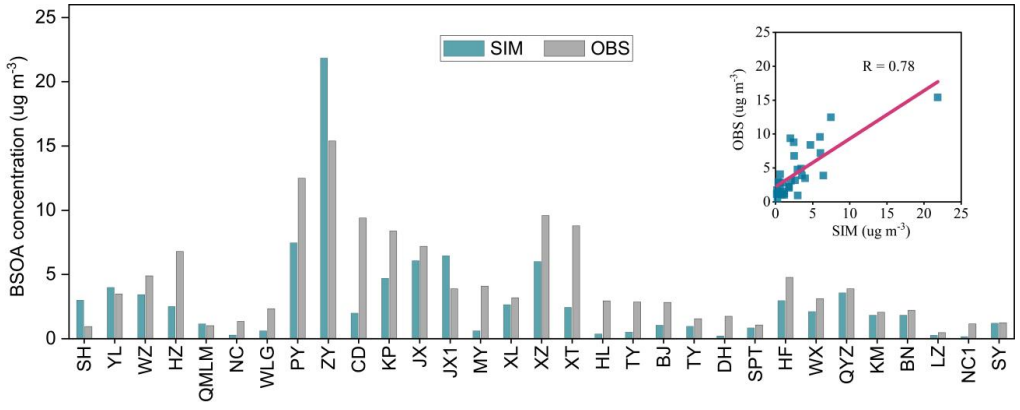

Figure 3 | Comparison of observed and simulated surface BSOA concentrations across China. Observed data (grey bars) from 29 sites are compiled from previous studies (Ding et al., 2014; Zhang et al., 2024; Zheng et al., 2017; Zhu et al., 2016; Zhang et al., 2018b; Xu et al., 2018; Zhang et al., 2019; Qin et al., 2017; Hu et al., 2016; Hu et al., 2013; Huang et al., 2011; Huang et al., 2013; Du et al., 2015; Li et al., 2020a; Wang et al., 2016b; Zhang et al., 2018a). Simulated BSOA concentrations (green bars) represent 2018-2020 model results at corresponding locations. The correlation coefficient between simulations and observations reaches 0.78, with good agreement evident in scatter plot.

3.3 Comparison with PFT-resolved model

Our species-resolved scheme (Exist-SPE) estimated annual BVOC emissions at 30.28 Tg in China, consisting of 9.27 Tg isoprene, 7.63 Tg monoterpenes, 0.53 Tg sesquiterpenes and 12.85 Tg other VOC species. Our estimated isoprene emissions fall within the reported range of 5.4-37.5 Tg yr^{-1} in existing literature, while monoterpene emissions align with the 2.66-7.64 Tg yr^{-1} range (Table 2; Gao et al., 2025; Cao et al., 2018; Li et al., 2023; Li and Xie, 2014; Wang et al., 2021; Stavrakou et al., 2014; Fu and Liao, 2012; Li et al., 2013; Wu et al., 2020; Ma et al., 2023; Li et al., 2020b; Cao et al., 2024; Wang et al., 2025). Notably, monoterpenes account for 25.2% of total emissions, exceeding values reported in most studies, which we attribute to the use of species-resolved algorithms (Xi et al., 2025; Li et al., 2025). Previous estimates were predominantly generated by MEGAN2.1 with PFT scheme, though some incorporated satellite-based inverse modeling for top-down constraints. Such PFT-based approaches overlook inter-species variability in emission potentials and thereby systematically bias emission flux estimates. Notably, Gao et al. employed the MEGAN v3 model and provided both national and forest-scale estimates for China, offering a consistent basis for cross-scale evaluation. In national scale, total BVOC emissions in this study align with Gao et al. (29.57 Tg yr^{-1}), with lower isoprene (9.27 vs. 12.56 Tg yr^{-1}) and closer monoterpenes (7.63 vs. 7.64 Tg yr^{-1}) fluxes. Across ecosystem types, forests accounted for 30.8% of national BVOC emissions (10.26 Tg yr^{-1}), followed by other woodlands (canopy closure < 0.2) contributing 28.1%, shrublands 17.9%, grasslands 13.2%, and croplands 9.8%. For forests specifically, our results show more monoterpenes emission than those reported by Cao et al (2018) (isoprene: 3.57 vs. 3.90 Tg yr^{-1}; monoterpenes: 3.12 vs. 1.97 Tg yr^{-1}).

Moreover, incorporating species-specific emission factors refined BVOC estimates for China's forests, with the Exist-SPE yielding total emissions of 10.26 Tg yr^{-1} in 2019, representing a 16.2% reduction relative to the Exist-PFT estimate of 12.25 Tg yr^{-1} (Fig. 4a). This discrepancy was primarily driven by isoprene and monoterpenes, contributing 1.06 and 1.12 Tg yr^{-1} respectively (Fig. 4b, 4c), whereas sesquiterpenes accounted for only 0.03 Tg yr^{-1} given their intrinsically low emission. In contrast, other VOCs were 0.20 Tg yr^{-1} higher in Exist-SPE than its PFT-based

https://doi.org/10.5194/egusphere-2026-3708
Preprint. Discussion started: 10 July 2026

counterpart. Spatially, Exist-PFT exhibited widespread overestimation across most forested regions in China (Fig. 4a). For instance, the average isoprene emission factor for temperate evergreen needleleaf forests is 2.45 nmol m^{-2} s^{-1} in Exist-PFT, whereas species-level refinement gives a much lower value of 0.39 nmol m^{-2} s^{-1} for the dominant species, e.g., *Pinus massoniana*. A similar pattern is observed in temperate broadleaf forests, whose emission factor is 40.85 nmol m^{-2} s^{-1} in Exist-PFT, largely exceeding the refined value of 18.01 nmol m^{-2} s^{-1} for prevalent species such as *Quercus mongolica*. Underestimation of emission factor in Exist-PFT was confined mostly in southwestern and central-eastern regions. For isoprene specifically (Fig. 4b), underestimation in southwestern China was associated with *Quercus liaotungensis* stands (species-specific emission factor: 34.0 nmol m^{-2} s^{-1} vs. PFT-resolved emission factor: 7.45 nmol m^{-2} s^{-1}), while in central China, it occurred across *Quercus variabilis* forests in the northern part of this region (25.0 vs. 12.60 nmol m^{-2} s^{-1}) and *Quercus serrata* forests in the central part (25.4 vs. 12.34 nmol m^{-2} s^{-1}). In eastern China, mixed woodlands comprising *Quercus chenii* (34.0 nmol m^{-2} s^{-1}), *Quercus serrata* (25.4 nmol m^{-2} s^{-1}), *Robinia pseudoacacia* (20.0 nmol m^{-2} s^{-1}), and *Quercus glauca* (94.7 nmol m^{-2} s^{-1}) collectively exceeded the Exist-PFT emission factor of 11.50 nmol m^{-2} s^{-1}. Additionally, *Phyllostachys edulis* plantations (23.65 nmol m^{-2} s^{-1} vs. PFT: 11.50 nmol m^{-2} s^{-1}) across several provinces reinforced this pattern in southeastern China.

The incorporation of species-level data accentuated the spatial heterogeneity of BVOC emissions, engendering sharper delineations and localized hotspots that mirror the intrinsic disparities among tree species. By comparison, the Exist-PFT simulations projected smoother gradients and seamless transitions, wherein emission intensities varied with latitudinal or climatic gradients. These discrepancies arise from intra-PFT averaging, which conflates species with variable emission factors into a default value, thereby obscuring the impacts of actual vegetation assemblages.

Table 2. BVOC emissions in China from previous and this Study (Tg)

Data Source	Isoprene	Monoterpene	Total	Study Period	Model
This Study	9.27	7.63	30.28	2019	MEGAN v3.2
Cao et al. (2018)	5.4-11.7		12.2-22.8	2007	inversion of satellite
Gao et al. (2025)	12.56	7.64	29.57	2019	MEGAN v3.2
Li et al (2023)	7.23	6.33	23.26	2014-2020	MEGAN v3.1
Li and Xie (2014)	27.09	6.32	48.5	1999-2003	MEGAN v2.1
Wang et al. (2021)	14.63-16.7	3.78-4.12	31.77-35.48	2001-2016	MEGAN v2.1
Stavrakou et al. (2014)	6.7-7.6			2007-2012	MEGAN v2.1
Stavrakou et al. (2014)	6.5-8.6			2007-2012	inversion of satellite
Fu and Liao. (2012)	10.87	3.21	21.36	2001-2006	MEGAN v2.0
Li et al. (2013)	23.42	5.55	42.54	2003	MEGAN v2.1
Wu et al. (2020)	13.3	3.09	23.54	2017	MEGAN v2.1
Ma et al. (2023)	12.1-22.73	2.66-4.19	25.42-37.39	2000-2017	MEGAN v2.1
Li et al. (2020b)	28.23-37.45	5.85-6.69	49.0-58.89	2018	MEGAN v2.1
Wang et al. (2025)	17.5		32.47	2020	MEGAN v2.1
This Study (forest)	3.57	3.12	10.26	2019	MEGAN v3.2
Cao et al. (2024; forest)	3.90	1.97	9.86	2020	MEGAN v3.1

https://doi.org/10.5194/egusphere-2026-3708
Preprint. Discussion started: 10 July 2026

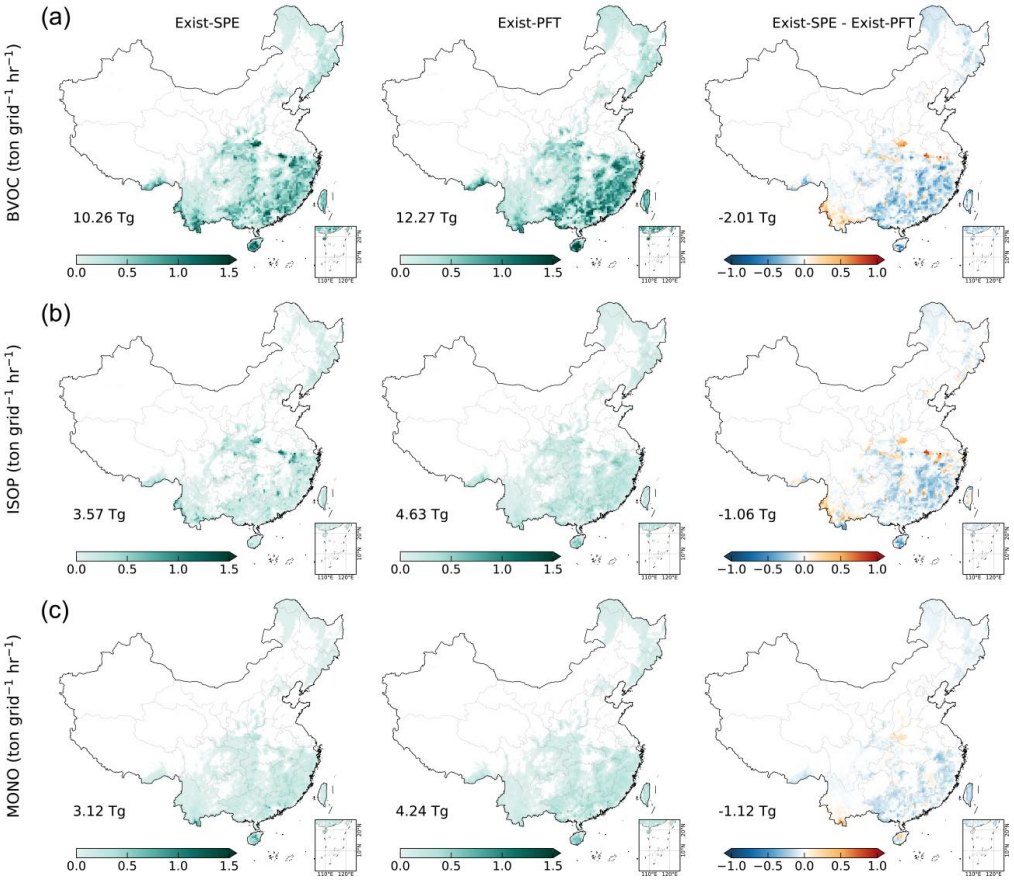

Figure 4. Spatial patterns of BVOC emissions in China under species-resolved and PFT-based schemes. Columns 1-3 show the annual mean emissions from the Exist-PEC, the Exist-PFT, and their difference, respectively. Rows 1-3 represent total BVOCs, isoprene, and monoterpenes, respectively.

4 Contributions of tree species to BVOC emissions

4.1 Characteristics of national BVOC emissions

We developed a high-resolution BVOC emissions inventory of forests in China using our enhanced input data and adjusted model (https://doi.org/10.5281/zenodo.20396128, Liu et al., 2026), integrating spatial distribution with species-level emission factors across 234 tree species (Table C4). The national annual BVOC emissions in 2019 are estimated at 10.26 Tg, which includes 3.57 Tg of isoprene, 3.12 Tg of monoterpenes, 0.18 Tg of sesquiterpenes, and 3.39 Tg of other VOC species (Table 2). *Pinus massoniana* occupies the most extensive area (19.71 Mha, 10.5% of total forested coverage; Fig. 5) and serves as the leading contributor to national forest BVOC emissions (1.68 Tg yr^{-1}; 16.4% of total emissions), primarily through monoterpene and sesquiterpene release (0.95 Tg yr^{-1}).

Spatially, BVOC emissions exhibit a south-to-north decreasing gradient, with the largest source concentrated in

https://doi.org/10.5194/egusphere-2026-3708
Preprint. Discussion started: 10 July 2026

the subtropical and tropical regions of southern China (Fig. 4a). In these regions, *Pinus massoniana*, *Quercus liaotungensis*, *Phyllostachys edulis* and *Cunninghamia lanceolata* are the primary BVOC-emitting species, with a combined planted area of 44.77 Mha and total emissions of 3.94 Tg yr^{-1}, driven largely by dense forest cover, elevated temperatures, and intense solar radiation (Fig. 5). In northeastern China, boreal forests dominated by species such as *Quercus mongolica* and *Larix gmelinii* (17.6 Mha), exhibit limited emission due to low temperatures and solar radiation, particularly during the winter. Emissions are also low in the western arid zones, primarily due to sparse forest cover. This spatial variability highlights the linkage between forest composition, regional climate conditions, and BVOC emission intensity, which together shape the geographic distribution of BVOC emissions.

Seasonally, national BVOC emissions exhibit pronounced temporal dynamics driven by the combined effects of temperature, solar radiation, and leaf area index. Summer (June-August) represents the dominant emission season, accounting for approximately 49.9% of the total emission under optimal meteorological and phenological phase, followed by autumn (22.7%, September-November), spring (21.2%, March-May), and winter (6.3%, December-February). This seasonal pattern manifests distinctly in the spatial distribution of emissions. During summer, elevated emissions occur across forests nationwide, reflecting broadly favorable growth and metabolic conditions. In winter, emissions from northern forests decline due to low temperatures and leaf senescence, whereas forests south of 35°N, predominantly composed of evergreen species, maintain comparatively high emission rates year-round. These spatiotemporal patterns highlight temperature and solar radiation as key drivers of vegetative metabolic activity, thereby shaping BVOC emission dynamics.

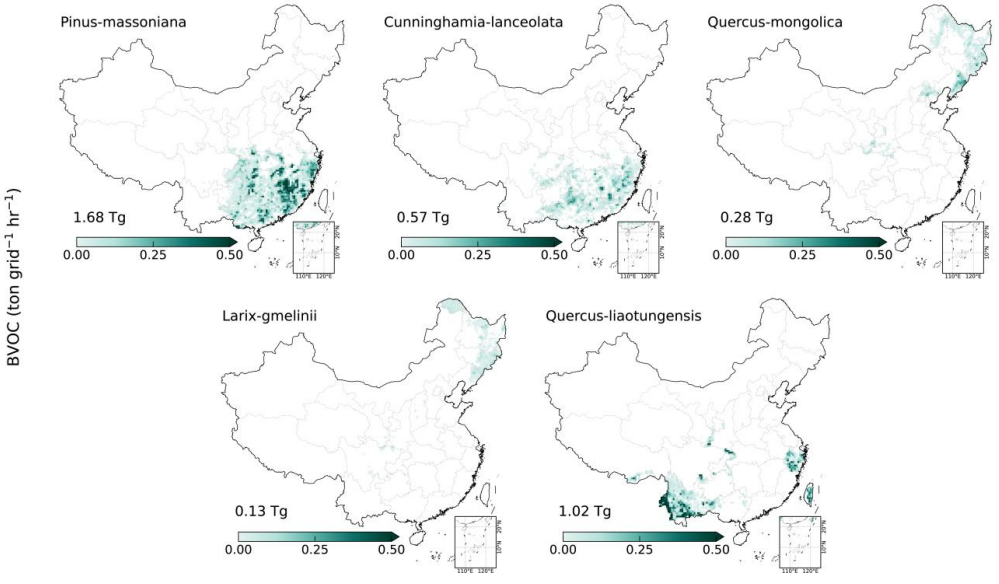

Figure 5 | Spatial distribution and BVOC emission characteristics of the five most widely distributed tree species in China. The five species ranked by forest area are *Pinus massoniana* (19.7 Mha), *Cunninghamia lanceolata* (12.3 Mha), *Quercus mongolica* (9.0 Mha), *Larix gmelinii* (8.6 Mha), and *Quercus liaotungensis* (7.98 Mha). Green shading indicates mean annual BVOC emission rates (ton $grid^{-1}$ hr^{-1}), and numbers denote total annual emissions (Tg).

https://doi.org/10.5194/egusphere-2026-3708
Preprint. Discussion started: 10 July 2026

4.2 BVOC emissions and species contributions

The top five species by area, including *Pinus massoniana* (19.7 Mha), *Cunninghamia lanceolata* (12.3 Mha), *Quercus mongolica* (9.0 Mha), *Larix gmelinii* (8.6 Mha), and *Quercus liaotungensis* (7.98 Mha), with these five species collectively account for 30.8% of China's forest area (Fig. 5), underscoring a concentrated species composition at the national scale. However, tree species dominance in terms of BVOC emissions shows a different pattern. The top five species contributing to national BVOC emissions, e.g., *Pinus massoniana* (1.68 Tg yr^{-1}), *Quercus liaotungensis* (1.02 Tg yr^{-1}), *Phyllostachys edulis* (0.66 Tg yr^{-1}), *Cunninghamia lanceolata* (0.57 Tg yr^{-1}), and *Quercus variabilis* (0.34 Tg yr^{-1}), collectively account for 41.7% of the BVOC emissions while occupying only 25.4% of the forested area (Fig. 6a). This disparity calls for attention to high-emitting species in forest management and atmospheric modeling, as they occupy a limited forest area yet account for a large fraction of national BVOC budgets. Compound-level contributions demonstrate clear interspecific variability. *Pinus massoniana* is characterized by a terpene-dominant profile, whereas *Quercus liaotungensis* and *Phyllostachys edulis* are strong isoprene emitters, reflecting unique biochemical characteristics inherent to each species. The role of any given species in the national BVOC budget is co-determined by its coverage area, inherent emission capacity, and the environmental context of its distribution, as illustrated by cases discussed below.

Pinus massoniana is the greatest contributor to China's forest BVOCs inventory (Fig. 6a), with total emissions reaching 1.68 Tg yr^{-1}, accounting for 16.4% of the national forest BVOC emissions, and is characterized by a terpene-dominant emission profile comprising monoterpenes (0.91 Tg yr^{-1}), sesquiterpenes (0.04 Tg yr^{-1}), other BVOCs (0.70 Tg yr^{-1}), and a negligible isoprene contribution (0.03 Tg yr^{-1}). With a distribution covering 19.7 Mha, equivalent to 10.5% of China's total forest area, *Pinus massoniana* provides the most extensive spatial coverage for BVOC emissions of any single species in the country (Fig. 5). Additionally, *Pinus massoniana* possesses inherently high emission rates, with isoprene and monoterpenes fluxes reaching 0.39 and 0.71 nmol m^{-2} s^{-1}, respectively. As an evergreen conifer without seasonal leaf abscission, *Pinus massoniana* sustains elevated BVOC fluxes year-round and reaches peak emissions in summer, unlike deciduous species that undergo substantial emission reductions during winter. Collectively, its extensive spatial coverage, favorable climatic setting, and high intrinsic emission capacity establish *Pinus massoniana* as the dominant contributor to China's national forest BVOC budget. The next two leading emitters are *Quercus liaotungensis* (1.02 Tg yr^{-1}) and *Phyllostachys edulis* (0.66 Tg yr^{-1}), both characterized by isoprene-dominant emission profiles. *Quercus liaotungensis* occurs across 7.98 Mha primarily in southwestern and eastern China (Fig 6b), driven by a high isoprene flux of 34 nmol m^{-2} s^{-1} alongside a minor monoterpenes flux of 0.3 nmol m^{-2} s^{-1}, yielding isoprene 0.74 Tg yr^{-1}, monoterpenes 0.13 Tg yr^{-1}, sesquiterpenes 0.01 Tg yr^{-1}, and other BVOCs 0.14 Tg yr^{-1}. *Phyllostachys edulis*, an often overlooked yet key emission source spanning 4.82 Mha in southeastern China (Fig. 6b), exhibiting a strong isoprene emission rate of 23.65 nmol m^{-2} s^{-1}, with isoprene dominating its emission budget at 0.50 Tg yr^{-1}. *Cunninghamia lanceolata* (0.57 Tg yr^{-1}) and *Quercus variabilis* (0.34 Tg yr^{-1}) complete the list of the top five contributors. The role of any given species in the national BVOC budget is co-determined by its coverage area, inherent emission capacity, and the environmental context of its distribution, of which a principle illustrated by *Quercus variabilis*, which occupies only 2.7 Mha of forested area yet accounts for 0.34 Tg yr^{-1} of BVOC emissions (Fig. 6b), a contribution driven primarily by its high isoprene emission factor of 25.02 nmol m^{-2} s^{-1}. By contrast, *Larix gmelinii* is distributed across 8.56 Mha of northern boreal forest but yields only 0.13 Tg yr^{-1} of total BVOC emissions (Fig. 5). This disparity arises from its low intrinsic isoprene emission factor (0.04 nmol m^{-2} s^{-1}) combined with the constraints of unfavorable environmental conditions, where low temperatures and limited solar

https://doi.org/10.5194/egusphere-2026-3708
Preprint. Discussion started: 10 July 2026

radiation suppress emission rates.

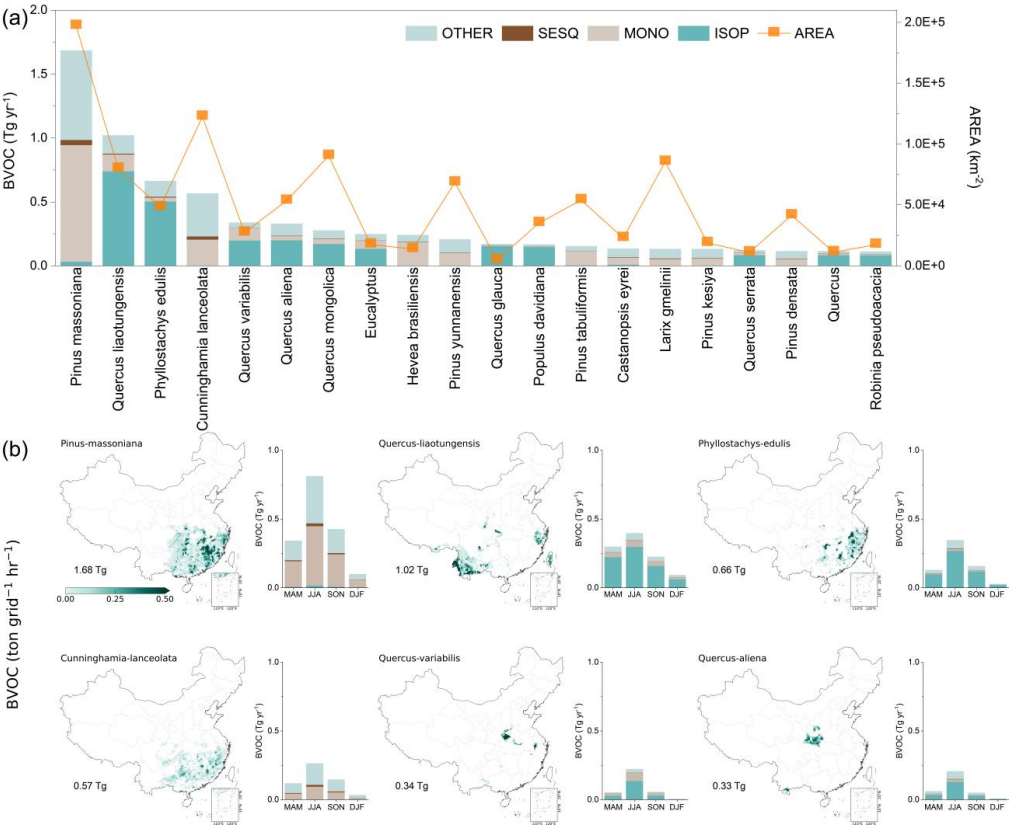

Figure 6 | BVOC emissions ranking at the tree species level in China. (a) Bar chart ranking the top 20 tree species by total BVOC emissions in 2019 (Tg yr^{-1}), with the yellow line denoting the total canopy coverage area (km^2) of each species. (b) Spatial distribution of BVOC emission rates (ton grid^{-1} hr^{-1}) for the six leading emitters: *Pinus massoniana*, *Quercus liaotungensis*, *Phyllostachys edulis*, *Cunninghamia lanceolata*, *Quercus variabilis*, and *Quercus aliena*, with annotated values representing total annual emissions in 2019 (Tg yr^{-1}). Inset bar charts show seasonal variation in BVOC emissions (Tg) across MAM (March-May), JJA (June-August), SON (September-November), and DJF (December-February).

Isoprene emissions across China's forests are dominated by broadleaf tree species. *Quercus liaotungensis* ranks as the largest contributor (Fig. 7), emitting 0.74 Tg yr^{-1} (20.7% of the national isoprene budget) from a distribution area of 7.98 Mha (4.3% of the national forest area) concentrated in southwestern and eastern China (Fig. 5), driven by a high emission factor of 34 nmol m^{-2} s^{-1}. *Phyllostachys edulis* follows closely, contributing 0.50 Tg yr^{-1} (14.0%) from 4.82 Mha (2.6%) across southeastern China, with an emission factor of 23.65 nmol m^{-2} s^{-1}. *Quercus aliena*, *Quercus variabilis*, and *Quercus mongolica* contribute 0.20 Tg yr^{-1} (5.6%), 0.20 Tg yr^{-1} (5.6%), and 0.17 Tg yr^{-1} (4.8%), respectively, with emission factors ranging from 13.16 to 25.02 nmol m^{-2} s^{-1} and distribution areas spanning central and northeastern China. Collectively, these five species account for 1.8 Tg yr^{-1} of isoprene emissions, representing 50.7% of the national total (3.57 Tg yr^{-1}; Fig. 7), while occupying only 15.9% of China's total forest area

https://doi.org/10.5194/egusphere-2026-3708
Preprint. Discussion started: 10 July 2026

(187.27 Mha). This striking contrast, with half of the national isoprene budget coming from less than one-sixth of the forest area, highlights the key role of a few high-emitting broadleaf species in shaping China's BVOC emissions.

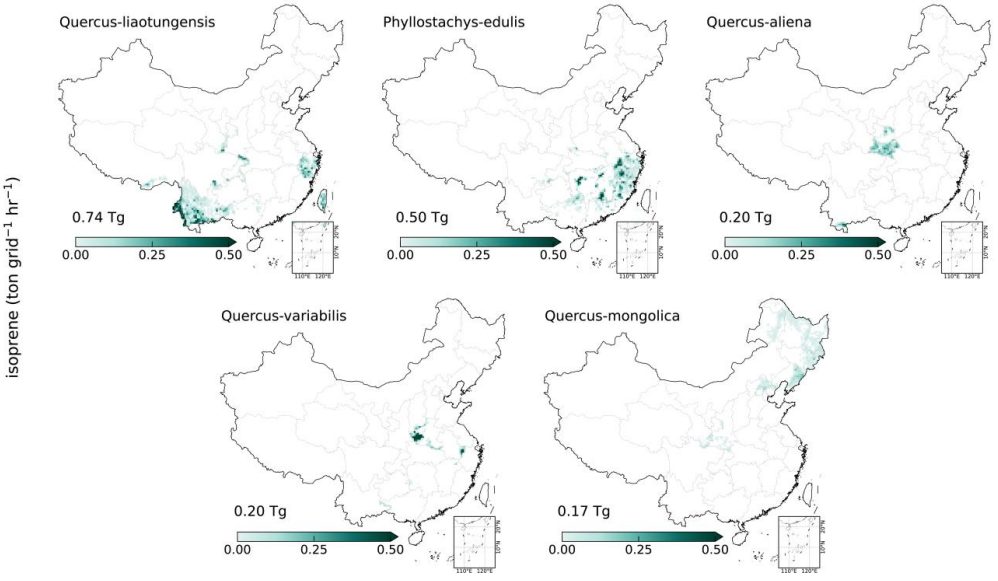

Figure 7 | Isoprene emission ranking at the tree species level in China. The five leading tree species ranked by isoprene annual emissions are *Quercus liaotungensis* (0.74 Tg yr^{-1}), *Phyllostachys edulis* (0.50 Tg yr^{-1}), *Quercus aliena* (0.20 Tg yr^{-1}), *Quercus variabilis* (0.20 Tg yr^{-1}), and *Quercus mongolica* (0.17 Tg yr^{-1}). Green shading indicates isoprene emission rates (ton grid^{-1} hr^{-1}), and numbers denote annual emissions (Tg).

Compared to isoprene, monoterpene emissions are dominated by coniferous species rather than broadleaf species. *Pinus massoniana* accounts for 0.91 Tg yr^{-1} (Fig. 8), representing nearly 30% of the national monoterpene budget, while occupying only 10.5% of China's total forest area (19.71 Mha) – a contribution enabled by its emission factor of 0.71 nmol m^{-2} s^{-1} and the warm, high-radiation conditions of southeastern China. *Cunninghamia lanceolata*, co-distributed in the same region across 12.26 Mha, contributes a further 0.20 Tg yr^{-1} (6.5%), reinforcing the geographic concentration of monoterpene emissions in southern China. Together, these two southeastern conifers represent over one-third of national monoterpene emissions (Fig. 8). Spatial extent alone is insufficient to explain monoterpene emissions among tree species. Although *Hevea brasiliensis* occupies only a small area of 1.37 Mha in tropical southern China, its high monoterpene emission factor of 2.22 nmol m^{-2} s^{-1}, results in a total emission (0.18 Tg yr^{-1}) comparable to that of *Cunninghamia lanceolata,* which distributes across nearly nine times the area (0.20 Tg yr^{-1}; 12.26 Mha). *Pinus tabuliformis* contributes 0.11 Tg yr^{-1} (3.6%) from 5.41 Mha with an emission factor of 1.66 nmol m^{-2} s^{-1}. Collectively, these five species emit 1.53 Tg yr^{-1}, accounting for 49.4% of the national monoterpene emissions while covering 24.8% of China's forest area (Fig. 8). Monoterpene budgets are governed primarily by conifers with high intrinsic terpene biosynthesis capacity, in contrast to the broadleaf and bamboo-dominated isoprene budget. This contrast underscores the necessity of compound-specific, species-resolved approaches in national BVOC inventory construction.

https://doi.org/10.5194/egusphere-2026-3708
Preprint. Discussion started: 10 July 2026

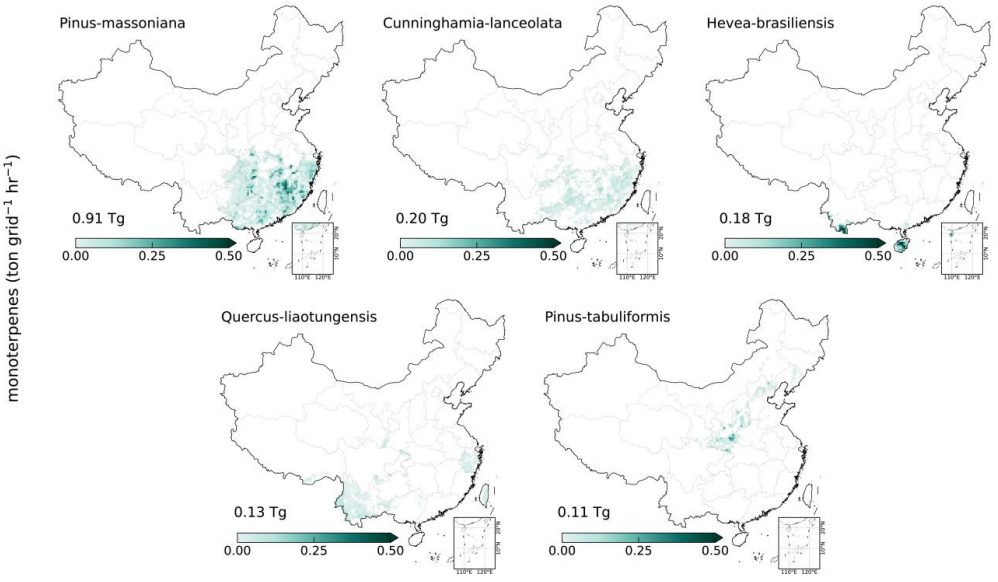

Figure 8 | Monoterpene emissions ranking at the tree species level in China. The five leading tree species ranked by monoterpene annual emissions are *Pinus massoniana* (0.91 Tg yr⁻¹), *Cunninghamia lanceolata* (0.20 Tg yr⁻¹), *Hevea brasiliensis* (0.18 Tg yr⁻¹), *Quercus liaotungensis* (0.13 Tg yr⁻¹), and *Pinus tabuliformis* (0.11 Tg yr⁻¹). Green shading indicates monoterpene emission rates (ton grid⁻¹ hr⁻¹), and numbers denote annual emissions (Tg).

4.3 Seasonal patterns of BVOC emissions

Seasonal variability in China's forest BVOC emissions is primarily governed by the differential responses of dominant tree species to temperature and solar radiation across seasons. During summer (Fig. 9), the five largest contributors to BVOC emissions are *Pinus massoniana* (0.81 Tg), *Quercus liaotungensis* (0.40 Tg), *Phyllostachys edulis* (0.35 Tg), *Cunninghamia lanceolata* (0.26 Tg), and *Quercus variabilis* (0.22 Tg), a ranking that mirrors the annual order given summer's dominant contribution to the yearly total. This consistency reflects the convergent influence of spatial coverage, intrinsic emission capacity, and climatic conditions. Specifically, evergreen conifers such as *Pinus massoniana* and *Cunninghamia lanceolata* sustain continuous BVOCs biosynthesis year-round, attaining highest emission rates when temperatures and solar radiation peak in summer. Meanwhile, isoprene-dominant deciduous species such as *Quercus liaotungensis*, *Phyllostachys edulis*, and *Quercus variabilis* reach peak emissions in summer, when leaf area reach seasonal maximum and high temperatures together with intense solar radiation stimulate isoprene biosynthesis.

In winter (Fig. 9), *Pinus massoniana* and *Quercus liaotungensis* remain the two largest contributors, yet their emissions decline by 87.7% and 77.5% relative to summer, falling to 0.10 and 0.09 Tg, respectively. Notably, *Hevea brasiliensis*, a minor contributor in summer (0.07 Tg), rises to the third largest emitter nationwide in winter (0.04 Tg). The low-latitude distribution of *Hevea brasiliensis* in tropical southern China experiences persistently high temperatures and solar radiation that sustain year-round metabolic activity, whereas emissions from high-latitude species decline. Examining the full annual emission cycle of individual species could further illustrate this latitudinal contrast. Temperate species north of 35°N exhibit pronounced seasonal variation, as exemplified by *Quercus variabilis*,

https://doi.org/10.5194/egusphere-2026-3708
Preprint. Discussion started: 10 July 2026

which allocates 66.0% of annual emissions to summer but only 1.4% to winter. By contrast, subtropical species such as *Hevea brasiliensis* show a more uniform seasonal distribution (spring 30.4%, summer 30.7%, autumn 23.3%, winter 15.6%), indicating that lower-latitude climatic conditions sustain BVOC emissions across seasons.

A clear seasonal shift is imprinted on emission composition. Isoprene constitutes 37.4% of seasonal BVOCs in summer but falls to 26.1% in winter, whereas monoterpenes rise from 28.4% to 37.2%. Two primary factors contribute to this compositional divergence. Isoprene biosynthesis, proceeding via the methylerythritol phosphate pathway, exhibits higher sensitivity to both light intensity and leaf temperature than monoterpene synthesis, leading to greater production under summer conditions. In parallel, deciduous broadleaf isoprene emitters such as *Quercus variabilis* (EF: 25.02 nmol m^{-2} s^{-1}) further amplify this seasonal divergence. In summer (Fig. 9), developed leaf area combined with peak photosynthetic activity boosts isoprene production, whereas in winter, leaf abscission limits its isoprene flux, reducing the isoprene fraction of the seasonal emission.

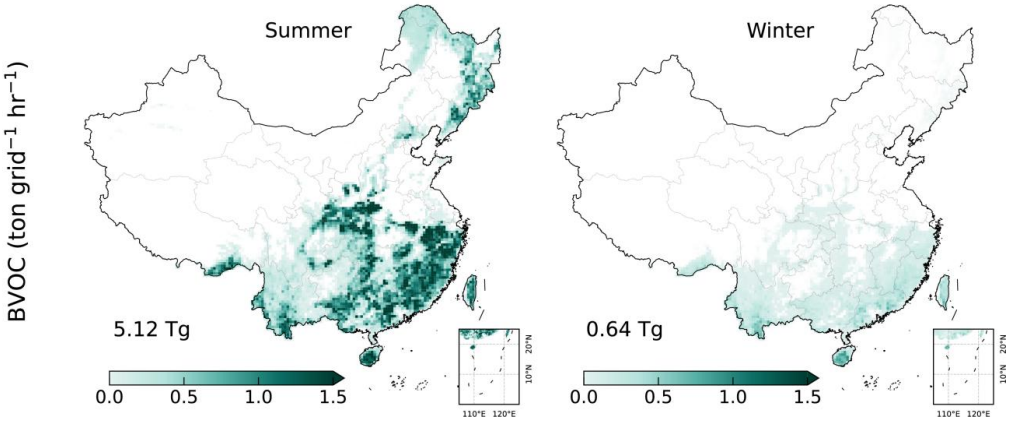

Figure 9 | Spatial distribution of BVOC emissions from forests in China during summer and winter. Green shading indicates gridded BVOC emission rates (ton $grid^{-1}$ hr^{-1}), with seasonal emissions reaching 5.12 Tg during summer (JJA) and 0.64 Tg during winter (DJF), reflecting the strong seasonal contrast driven by temperature and radiation conditions across China's forest ecosystems.

5 BVOC contributions under A&R scenarios

5.1 BIO scenario

In the BIO scenario, the 78 Mha area designated for A&R is converted to plantation forests optimized for biomass accumulation, driving a national BVOC emission increment of 4.65 Tg yr^{-1} (Fig. 10), which marks a 45.3% increase compared to the existing forests (10.26 Tg yr^{-1}). This incremental emission consists of isoprene at 1.72 Tg yr^{-1}, monoterpenes at 1.29 Tg yr^{-1}, sesquiterpenes at 0.08 Tg yr^{-1}, and other VOCs at 1.55 Tg yr^{-1}. The BIO plantations are dominated by deciduous broadleaf forests concentrated in southeastern China (35.7%) and evergreen broadleaf forests in the southwestern region (31.8%). The five most extensively planted species including *Cunninghamia lanceolata* (8.65 Mha; Fig. B1), *Quercus aquifolioides* (8.43 Mha), *Camellia sinensis* (4.70 Mha), *Juglans* (3.20 Mha), and *Castanopsis delavayi* (2.65 Mha) collectively account for 35.7% of the A&R area (78 Mha). Although *Cunninghamia lanceolata* covers the largest area (10.9%), it is not the dominant emitter of BVOCs, primarily due to low emission

https://doi.org/10.5194/egusphere-2026-3708
Preprint. Discussion started: 10 July 2026

rates for isoprene (0.01 nmol m^{-2} s^{-1}) and monoterpenes (0.33 nmol m^{-2} s^{-1}).

Among all planted species in the BIO scenario, *Quercus aquifolioides*, concentrated predominantly in southwestern China across 8.43 Mha, emerges as the single largest contributor at 0.47 Tg yr^{-1} (Fig. B2), with isoprene accounting for approximately 69.4% and monoterpenes for 14.7%. In contrast, *Cunninghamia lanceolata* – the most widely planted species at 8.65 Mha across southern China – contributes 0.37 Tg yr^{-1} and ranks second overall (Fig. B2), consistent with its low emission factors (isoprene: 0.01 nmol m^{-2} s^{-1}; monoterpenes: 0.33 nmol m^{-2} s^{-1}). *Quercus liaotungensis* (Fig. B2), despite occupying only 1.84 Mha, contributes total emissions of 0.34 Tg yr^{-1} (isoprene: 0.25 Tg yr^{-1}; monoterpenes: 0.04 Tg yr^{-1}), attributable to its high leaf-level emission factors for isoprene (34 nmol m^{-2} s^{-1}) and monoterpenes (0.3 nmol m^{-2} s^{-1}).

From a spatial perspective, the incremental BVOC emissions following BIO scenario exhibit regional heterogeneity, with high-emission hotspots concentrated in southwestern and southern China (Fig. 10). This pattern is governed by the spatial distribution of high-emitting species. In southwestern China, extensive plantations of *Quercus aquifolioides* with high emission factors for isoprene (34 nmol m^{-2} s^{-1}) and monoterpenes (0.3 nmol m^{-2} s^{-1}), serving as the primary driver of elevated regional emissions (Fig. B2). South-central China constitutes another major emission center, where mixed deciduous broadleaf forests dominated by *Quercus* contribute to regional BVOC fluxes. Further south, tropical southern China emerges as a localized hotspot, attributable to the deployment of other deciduous broadleaf forest types with comparatively elevated emission capacities (12 nmol m^{-2} s^{-1} of isoprene; 0.3 nmol m^{-2} s^{-1} of monoterpenes).

5.2 SUIT scenario

The SUIT scenario prioritizes needleleaf and mixed forest types selected for ecological resilience, with afforestation designed to optimize species-environment matching. This strategy results in a national BVOC emission increase of 5.10 Tg yr^{-1} (Fig. 10), comprising isoprene (1.21 Tg yr^{-1}), monoterpenes (1.99 Tg yr^{-1}), sesquiterpenes (0.09 Tg yr^{-1}), and other VOCs (1.81 Tg yr^{-1}). In contrast to the BIO scenario, monoterpenes become the dominant component, indicating that the compositional shift arises from the forest-type configuration and associated species assemblages. Warm Pinaceae forests constitute the largest share (17.5%), followed by other deciduous broadleaf forests (16.8%), Betula-Populus forests (11.6%), and *Pinus massoniana* forests (9.40%), collectively distributed across the 78 Mha afforestation area. At the species level, conifers dominate the five most extensively planted taxa (Fig. B3): *Pinus yunnanensis* (8.91 Mha), *Pinus massoniana* (7.32 Mha), *Pinus tabuliformis* (4.05 Mha), and *Pinus armandii* (3.23 Mha), with *Betula platyphylla* (4.09 Mha) as the primary broadleaf counterpart.

The resulting emission structure is governed by the combined effects of species-specific emission factors and regional climatic conditions. Among all planted species in the SUIT scenario, *Pinus massoniana*, widely distributed in southeastern China, emerges as the largest BVOC contributor (0.76 Tg yr^{-1}; Fig. B4), with emissions dominated by monoterpenes (0.43 Tg yr^{-1}), reflecting both high emission factors (isoprene: 0.39 nmol m^{-2} s^{-1}; monoterpenes: 0.71 nmol m^{-2} s^{-1}) and the warm climatic conditions that sustain elevated BVOC biosynthesis. In contrast, *Pinus yunnanensis*, covering a larger area (8.91 Mha) yet contributing only 0.56 Tg yr^{-1}, primarily due to its high-elevation, low-temperature habitat in southwestern China that suppresses leaf-level BVOC synthesis. Meanwhile, *Eucalyptus* ranks third (0.41 Tg yr^{-1}), with emissions dominated by isoprene (0.22 Tg yr^{-1}), driven by a high isoprene emission factor (16 nmol m^{-2} s^{-1}), thereby decoupling emission contribution from planted area. Under the SUIT scenario, emission hotspots are concentrated in south-central and tropical southern China (Fig. 10). In south-central China,

https://doi.org/10.5194/egusphere-2026-3708
Preprint. Discussion started: 10 July 2026

Liquidambar formosana plantations generate elevated isoprene fluxes, whereas in tropical southern China, extensive *Eucalyptus* plantations (1.91 Mha) produce 0.29 Tg yr^{-1}, supported by an isoprene emission factor reaching 16 nmol m^{-2} s^{-1} and favorable tropical climatic conditions, forming a secondary emission center.

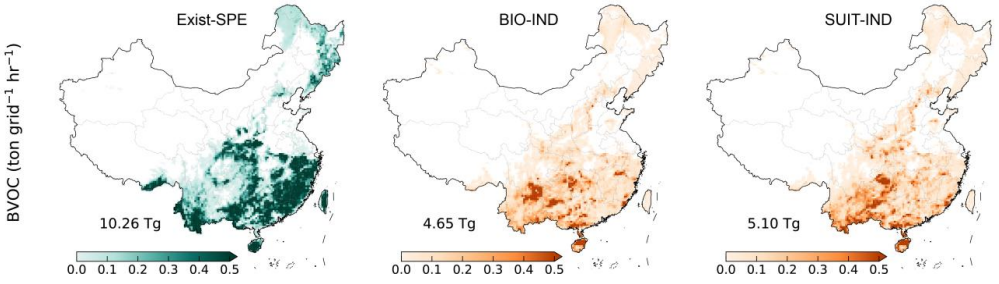

Figure 10 | Spatial patterns of BVOC emission increases under BIO and SUIT scenarios. Green shading indicates the spatial distribution of BVOC emission rates (ton $grid^{-1}$ hr^{-1}) from existing forest species (Exist-SPE), while yellow shading denotes the incremental BVOC emission rates attributable to A&R. Annotated values represent the annual BVOC emissions from Exist-SPE in 2019 and the corresponding emission increases under the BIO (4.65 Tg yr^{-1}) and SUIT (5.10 Tg yr^{-1}) scenarios, respectively.

6 Conclusion and Discussion

This study develops a species-resolved enhancement of the MEGAN framework for estimating BVOC emissions from China's forests (https://doi.org/10.5281/zenodo.20396128, Liu et al., 2026), integrating four key improvements to the model inputs: a tree species distribution map derived from China Forest Vegetation Survey, a species-specific emission factor database compiled from 184 peer-reviewed studies, an updated MODIS LAI product (MCD15A2H), and a refined MODIS land cover classification (MCD12Q1). Applying this enhanced framework, we construct a species-resolved BVOC emission inventory for 234 dominant tree species across China's forests in 2019, estimating total forest BVOC emissions at 10.26 Tg yr^{-1} with a south-to-north decreasing gradient and a summer peak accounting for ~50% of the annual total. The five largest contributors – *Pinus massoniana*, *Quercus liaotungensis*, *Phyllostachys edulis*, *Cunninghamia lanceolata*, and *Quercus variabilis* – collectively accounted for 41.7% of total emissions while occupying only 25.4% of the forested area, indicating that emission magnitude is co-determined by intrinsic emission capacity, spatial coverage, and local climatic conditions. Several sources of uncertainty warrant consideration in interpreting these results. First, tree age influences both the magnitude and composition of BVOC emissions (Tian et al., 2026), yet age-related variation was not considered here. Seedlings have been reported to emit ~50 % more isoprene and to be enriched in cyclic monoterpenes compared with mature trees (Tian et al., 2026). This limitation is particularly relevant for large-scale plantation forests, where trees are concentrated in active growth stages and age-dependent emission differences cannot be neglected. Second, the current model applies uniform stress-response parameterizations across all tree species, neglecting interspecific heterogeneity in BVOC emission responses to environmental stressors. Heat stress, for instance, converts beech from a negligible to an active isoprene emitter while suppressing isoprene emissions in oak (Dey et al., 2026), underscoring the risk of systematic bias from species-uniform stress-response parameterizations. Third, mixed-stand polygons were disaggregated using an equal-proportion assumption in the absence of species-level stocking data, which may introduce allocation bias in structurally complex mixed forests. Addressing these uncertainties requires expanded field measurements across age

https://doi.org/10.5194/egusphere-2026-3708
Preprint. Discussion started: 10 July 2026

classes and underrepresented species, alongside high-resolution forest inventory data resolving species-level composition.

Transitioning from PFT-level to species-resolved scheme represents an advance in biogenic emission modeling for China, enabling the detection of high-emitting species otherwise obscured by PFT averaging and yielding a more physically consistent representation of spatial emission heterogeneity. Our finding challenges the prevailing assumption that extensive forest area implies correspondingly high emissions – a misconception with non-trivial consequences for land management decisions. This insight reframes the interpretation of existing forest emissions and, by extension, the evaluation of planned afforestation. Because A&R programs inherently involve species selection, they determine the chemical composition of subsequent BVOC emissions. Specifically, the BIO scenario produces isoprene-dominated emission increments, whereas the SUIT scenario shifts the balance toward monoterpene-dominated emissions, reflecting the combined influence of species-specific emission factor profiles, tree species selection, and regional climate gradients on national-scale BVOC composition. These contrasting atmospheric chemistry footprints carry implications that extend beyond differences in total BVOC flux, encompassing secondary organic aerosol formation, tropospheric ozone chemistry, and regional air quality – underscoring the need to integrate species-resolved biogenic emission considerations into future afforestation policy design.

Appendix A

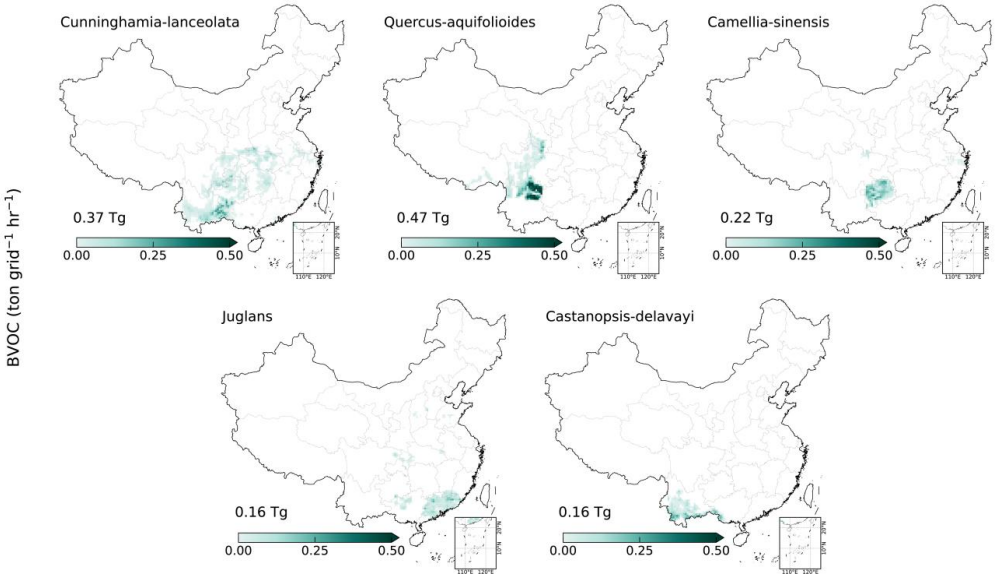

Figure B1 | Spatial distribution and BVOC emission characteristics of the five most widely distributed tree species in BIO scenario. The five species ranked by forest area are *Cunninghamia lanceolata* (8.65 Mha), *Quercus aquifolioides* (8.43 Mha), *Camellia sinensis* (4.70 Mha), *Juglans* (3.20 Mha), and *Castanopsis delavayi* (2.65 Mha). Green shading indicates the spatial distribution of afforestation-induced BVOC emission increments (ton grid^{-1} hr^{-1}), and numbers denote the annual increment in BVOC emissions attributable to A&R (Tg).

https://doi.org/10.5194/egusphere-2026-3708
Preprint. Discussion started: 10 July 2026

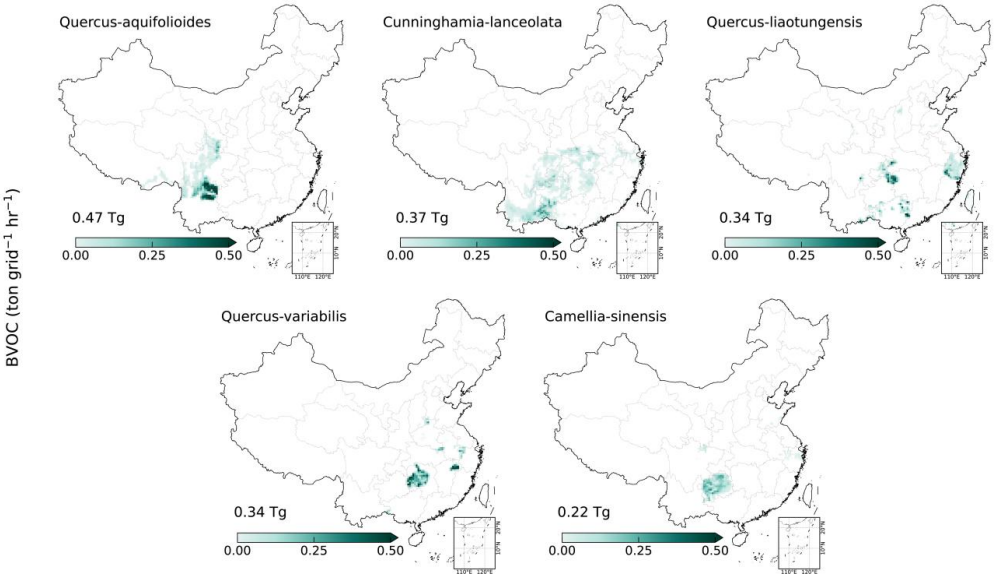

739

740 **Figure B2 | BVOC emissions ranking at the tree species level in BIO scenario.** Spatial distribution of afforestation-induced
741 BVOC emission increments (ton grid^{-1} hr^{-1}) for the five leading emitters: *Quercus aquifolioides*, *Cunninghamia lanceolata*,
742 *Quercus liaotungensis*, *Quercus variabilis*, and *Camellia sinensis*, with annotated values representing the annual increment in
743 BVOC emissions attributable to A&R (Tg yr^{-1}).

744

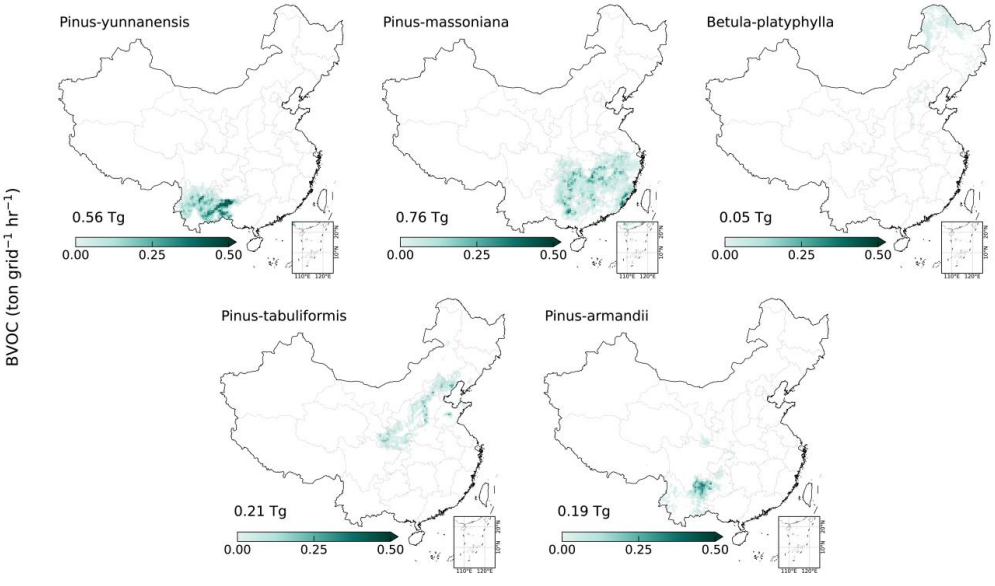

745

746 **Figure B3 | Spatial distribution and BVOC emission characteristics of the five most widely distributed tree species in SUIT**
747 **scenario.** The five species ranked by forest area are *Pinus yunnanensis* (8.91 Mha), *Pinus massoniana* (7.32 Mha), *Betula*
748 *platyphylla* (4.09 Mha), *Pinus tabuliformis* (4.05 Mha), and *Pinus armandii* (3.23 Mha). Green shading indicates the spatial
749 distribution of afforestation-induced BVOC emission increments (ton grid^{-1} hr^{-1}), and numbers denote the annual increment in

https://doi.org/10.5194/egusphere-2026-3708
Preprint. Discussion started: 10 July 2026

BVOC emissions attributable to A&R (Tg yr^{-1}).

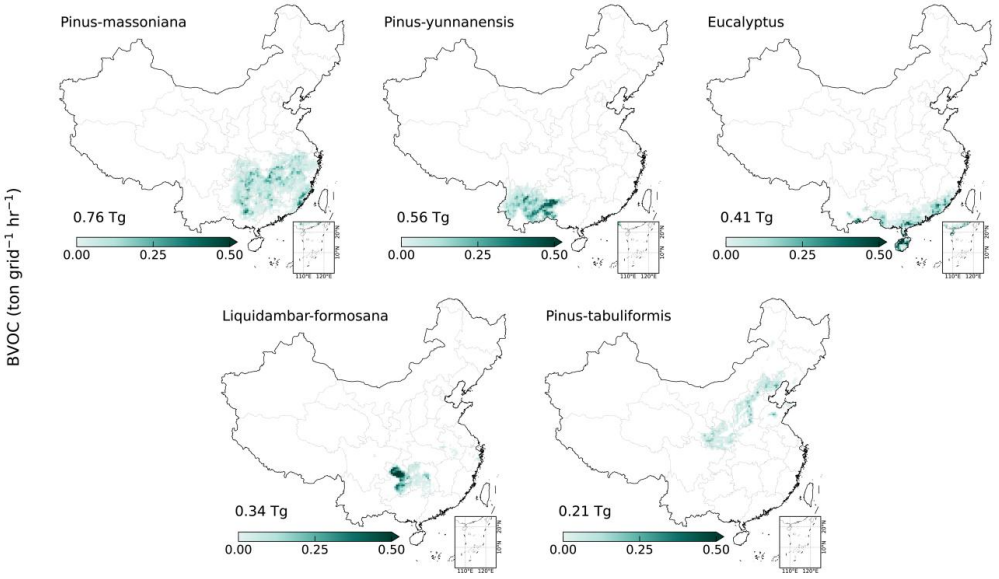

Figure B4 | BVOC emissions ranking at the tree species level in SUIT scenario. Spatial distribution of afforestation-induced BVOC emission increments (ton $grid^{-1}$ hr^{-1}) for the five leading emitters: *Pinus massoniana*, *Pinus yunnanensis*, *Eucalyptus*, *Liquidambar formosana*, and *Pinus tabuliformis*, with annotated values representing the annual increment in BVOC emissions attributable to A&R (Tg yr^{-1}).

Table C1. Evaluation of predicted vs. observed LAI

Month	Pred	Obs	Bias	r	RMSE	MAE
Jan	27.01	22.33	4.68	0.65	16.52	10.67
Feb	26.87	21.17	5.69	0.62	16.85	10.85
Mar	31.14	25.61	5.53	0.69	17.24	10.43
Apr	34.95	31.48	3.48	0.75	15.76	9.46
May	41.26	35.65	5.61	0.73	16.34	10.33
Jun	48.75	45.75	3.00	0.74	15.86	10.62
Jul	58.80	52.76	6.04	0.74	16.44	11.19
Aug	60.45	57.10	3.34	0.72	15.59	10.75
Sep	50.84	48.65	2.19	0.72	15.59	10.01
Oct	38.28	35.55	2.73	0.73	15.46	9.64
Nov	34.24	29.64	4.60	0.76	16.02	9.73
Dec	29.05	25.45	3.60	0.68	17.30	11.31

https://doi.org/10.5194/egusphere-2026-3708
Preprint. Discussion started: 10 July 2026

Table C2. Overview of WRF-Chem configurations

Physical and Chemical Options	Parameterization scheme
Spatial resolution	27 km
Microphysics	Morrison 2-mom
Cumulus	Grell-3
Planetary boundary layer	MYNN2
Longwave radiation	RRTMG
Shortwave radiation	RRTMG
Surface layer	MYNN
Land surface	CLM4
Gas-phase chemistry	MOZART
Aerosol module	MOSAIC with aqueous chemistry

Table C3. Comparison of simulated and observed BVOCs at four stations.

	Site	isoprene		monoterpenes	
		Exist-SPE	Exist-PFT	Exist-SPE	Exist-PFT
MB	DZ	0.77	1.74	-0.10	-0.77
	QYZ	0.58	1.88	0.29	0.49
	LA	2.06	1.22	0.39	0.96
	CBS	0.71	0.27	0.27	0.30
RMSE	DZ	1.23	2.24	2.90	2.91
	QYZ	0.68	2.09	0.63	0.76
	LA	2.96	2.01	0.48	1.19
	CBS	1.19	0.97	0.35	0.38

MB denotes mean bias, RMSE denotes root mean square error, Exist-SPE represents the species-level approach, and Exist-PFT represents the traditional plant functional type approach.

Table C4. BVOC emission factors for individual tree species

Dominant species or Forest type	isoprene (nmol m^{-2} s^{-1})	monoterpenes (nmol m^{-2} s^{-1})
Pinus massoniana	0.39	0.71
Cunninghamia lanceolata	0.01	0.33
Larix gmelinii	0.04	0.34
Larix gmelinii Rupr.	0.04	0.34
Quercus mongolica	18.01	0.10
Quercus liaotungensis	34.00	0.30
Pinus yunnanensis	0.00	0.45

https://doi.org/10.5194/egusphere-2026-3708
Preprint. Discussion started: 10 July 2026

Pinus tabuliformis	0.93	1.66
Betula platyphylla	0.00	0.15
Quercus aliena	13.16	0.12
Phyllostachys edulis	23.65	0.08
Pinus densata	0.00	0.45
Picea asperata	10.50	0.16
Quercus variabilis	25.02	0.74
Populus spp.	37.00	0.07
Populus davidiana	50.03	0.01
Castanopsis eyrei	0.79	0.30
Quercus aquifolioides	34.00	0.30
Cupressus funebris	0.00	0.70
Robinia pseudoacacia	20.00	0.05
Pinus kesiya	0.00	0.45
Eucalyptus	16.00	0.50
Abies fargesii	0.10	0.20
Camellia oleifera	0.11	0.03
Castanopsis fargesii	0.00	0.30
Hevea brasiliensis	0.09	2.22
Citrus	0.00	0.40
Picea likiangensis	5.91	0.35
Betula	0.00	0.15
Quercus spp.	34.00	0.30
Castanea seguinii	0.00	0.30
Betula dahurica	0.00	0.15
Abies	0.10	0.20
Quercus serrata	25.38	0.30
Pinus armandii	0.03	0.78
Pinus sylvestris	0.01	1.20
Paulownia	0.00	0.15
Picea spinulosa	5.00	0.35
Schima superba	0.00	0.20
Tilia tuan	0.00	0.20
Acer pictum	0.00	0.13
Fraxinus mandshurica	0.00	0.01
Bambusoideae	12.00	0.08
Pinus koraiensis	0.01	0.02
Pinus elliottii	0.00	0.45
Pinus hwangshanensis	0.00	0.45

https://doi.org/10.5194/egusphere-2026-3708
Preprint. Discussion started: 10 July 2026

Malus	0.00	0.04
Juniperus tibetica	0.01	0.36
Ulmus pumila	0.01	0.06
Camellia sinensis	7.10	0.03
Acacia confusa Merr.	0.62	0.30
Abies georgei	0.10	0.20
Populus tomentosa	61.53	0.08
Tsuga dumosa	0.00	0.60
Populus euphratica	37.00	0.07
Tsuga	0.00	0.60
Juglans	0.00	0.20
Castanopsis carlesii	0.00	0.30
Castanopsis calathiformis	0.00	0.30
Castanea mollissima	0.00	0.30
Juglans mandshurica	0.00	0.20
Liquidambar formosana	33.00	0.40
Castanopsis sclerophylla	0.00	0.30
Illicium verum	0.01	0.01
Cupressus torulosa	0.00	0.70
Phellodendron amurense	0.00	0.40
Populus ussuriensis	37.00	0.07
Larix principis-rupprechtii	0.04	0.13
Alnus nepalensis	0.00	0.02
Castanopsis delavayi	0.00	0.30
Abies delavayi sp. motuoensis	0.10	0.20
Cryptomeria	0.01	0.86
Terminalia myriocarpa	0.01	0.10
Quercus chenii	34.00	0.30
Pyrus communis	0.00	0.20
Prunus persica	0.00	0.50
Broadleaf Deciduous Boreal (Quercus)	14.00	0.30
Alnus cremastogyne	0.00	0.02
Litchi chinensis	0.01	0.45
Betula utilis	0.00	0.15
Pinus thunbergii	0.00	0.45
Quercus glauca	94.70	0.33
Platycladus orientalis	0.05	0.49
Betula costata	0.00	0.15
Cryptocarya concinna	10.70	3.01

https://doi.org/10.5194/egusphere-2026-3708
Preprint. Discussion started: 10 July 2026

Castanopsis chinensis	0.00	0.04
Castanopsis tonkinensis	0.00	0.30
Evergreen Cunninghamia lanceolata	0.01	0.33
Pinus densiflora	0.00	0.68
Toona ciliata	0.00	0.08
Quercus semecarpifolia	34.00	0.30
Lannea coromandelica	0.00	0.60
Vernicia fordii	0.02	0.00
Cyclobalanopsis glaucoides	94.70	0.33
Castanopsis fargesil	0.00	0.30
Ziziphus jujuba	11.75	0.16
Larix potaninii	0.00	0.30
Pistacia chinensis	1.00	0.10
Albizia kalkora	2.00	0.25
Larix mastersiana	0.00	0.30
Pseudolarix amabilis	0.00	0.45
Mangifera indica	32.50	0.60
Cinnamomum camphora	0.00	0.00
Zanthoxylum bungeanum	10.00	0.10
Salix	37.00	0.10
Bambusa emeiensis	12.00	0.08
Picea likiangensis E.Pritz.	5.91	0.35
Prunus mume	0.00	0.50
Morus	0.00	0.10
Fargesia	12.00	0.08
Juniperus sabina	0.00	0.39
Dacrycarpus imbricatus	0.00	0.45
Dacrydium pectinatum	0.00	0.45
Magnolia	0.00	0.20
Pterocarya stenoptera	0.00	0.08
Eucommia ulmoides	4.35	0.05
Crataegus pinnatifida	0.00	0.10
Eucalyptus maidenii	16.00	0.50
Betula alnoides	0.00	0.15
Pinus wallichiana	0.00	2.42
Evergreen Pinus	0.80	0.50
Rhus chinensis	5.00	0.60
Lindera glauca	0.00	0.12
Lithocarpus glaber	0.00	0.30

https://doi.org/10.5194/egusphere-2026-3708
Preprint. Discussion started: 10 July 2026

Pinus palustris	0.00	0.45
Populus nigra	45.30	0.21
Acacia confusa	0.10	0.30
Phoebe sheareri	0.00	0.12
Cinnamomum pedunculatum	0.00	0.00
Ginkgo biloba	0.01	0.44
Dalbergia hupeana	7.03	0.30
Quercus fabri	21.47	0.30
Keteleeria	0.01	0.33
Larix kaempferi	0.04	0.34
Ficus microcarpa	16.00	0.08
Phyllostachys reticulata	23.65	0.08
Dendrocalamus latiflorus	12.00	0.08
Bambusa sinospinosa	12.00	0.08
Pinus taiwanensis	0.00	0.45
Saraca Dysoxylum Eberhardtia	12.00	0.30
Eucalyptus grandis	22.69	0.19
Betula luminifera	0.01	0.15
Populus adenopoda	37.00	0.07
Sorbus	0.00	0.05
Diospyros	0.00	0.10
Casuarina	30.00	0.32
Castanea henryi	0.00	0.30
Populus szechuanica	37.00	0.07
Metasequoia glyptostroboides	0.00	0.30
Betula albosinensis	0.00	0.15
Idesia polycarpa	37.00	0.10
Prunus sect	0.00	0.50
Quercus acutissima	0.02	0.30
Canarium album	2.31	0.05
Cyclobalanopsis oxyodon myrsinifolia	94.70	0.33
Cotinus coggygria	0.00	0.60
Houpoea officinalis	0.02	0.06
Pinus caribaea	0.00	0.45
Dendrocalamus giganteus	12.00	0.08
Pinus latteri	0.00	0.45
Phoebe zhennan	0.00	0.12
Prunus americana	0.00	0.50
Taiwania flousiana	0.01	0.33

https://doi.org/10.5194/egusphere-2026-3708
Preprint. Discussion started: 10 July 2026

Platyosprion platycarpum	10.00	0.16
Osmanthus fragrans	0.04	0.00
Sapium sebiferum	0.00	0.15
Elaeagnus angustifolia	8.00	0.20
Pinus taeda	0.00	0.45
Ilex	0.10	0.20
Eucalyptus globulus	23.82	1.35
Fagus longipetiolata	0.00	0.15
Melia azedarach	0.00	0.03
Platycarya strobilacea	0.00	0.40
Eucalyptus robusta	38.30	0.89
Abies squamata	0.10	0.20
Paulownia fargesii	0.00	0.15
Fraxinus chinensis	0.25	0.02
Moso bamboo	23.65	0.08
Abies delavayi	0.10	0.20
Dendrocalamus	12.00	0.08
Alnus japonica	0.00	0.02
Prunus sibirica	0.00	0.50
Sassafras tzumu	0.00	0.03
Carpinus turczaninowii	0.00	0.02
Cornus controversa	0.50	0.03
Picea crassifolia	5.00	0.35
Christmas tree	12.00	0.30
Populus lasiocarpa	0.00	0.20
Dimocarpus longan	0.86	0.10
Quercus stewardii	34.00	0.30
Camphora septentrionalis	0.00	0.00
Quercus variabilis Blume	13.16	0.12
Phyllostachys heteroclada	23.65	0.08
Machilus-Castanopsis	0.00	0.12
Kandelia obovata	12.00	0.19
Populus alba var. pyramidalis	37.00	0.07
Eucalyptus urophylla	8.59	0.09
Styphnolobium japonicum	6.02	0.03
Phyllostachys bambusoides f. shouzhu	23.65	0.08
Camptotheca acuminata	30.00	0.08
Kalopanax septemlobus	12.00	0.30
Phyllostachys bissetii	23.65	0.08

https://doi.org/10.5194/egusphere-2026-3708
Preprint. Discussion started: 10 July 2026

Phyllostachys glauca	23.65	0.08
Chimonobambusa quadrangularis	12.00	0.08
Toona sinensis	0.00	0.08
Pinus henryi	0.00	0.45
Leucaena leucocephala	0.00	0.01
Cyclobalanopsis multinervis	94.70	0.33
Coffea	0.00	0.15
Phyllostachys reticulata	23.65	0.08
Punica granatum	0.01	0.03
Rhus verniciflua	5.00	0.60
Pseudotsuga sinensis	0.00	0.20
Machilus	0.00	0.12
Trachycarpus fortunei	24.32	0.15
Prunus pseudocerasus	0.00	0.50
Taxus wallichiana	8.00	0.15
Pyrus betulifolia	0.00	0.20
Pleioblastus amarus	12.00	0.08
Styphnolobium japonicum Schott	6.02	0.03
Drepanostachyum fractiflexum	12.00	0.08
Eriobotrya japonica	1.00	0.10
Vachellia	0.00	2.00
Macadamia integrifolia	12.00	0.30
Ternstroemia gymnanthera	0.01	0.20
Cornus walteri	0.50	0.03
Larix speciosa	0.00	0.30
Rhizophora stylosa	0.00	0.07
Xanthoceras	0.00	0.12
Other evergreen coniferous forests	0.80	0.50
Other evergreen broad-leaved forests	12.00	0.30
Other Broadleaf Evergreen forests	10.00	0.30
Other Broadleaf Deciduous Tree	12.00	0.30
Broadleaf Deciduous Tree	8.00	0.30
Broadleaf Evergreen Tree	12.00	0.30

Data availability

The 1:1000000 forest type vector map from the 2013-2017 forest inventory is available at http://www.doi.org/10.12041/geodata.43370179401687.ver1.db (Chen et al., 2020). The MODIS Land Cover Type product (MCD12Q1) is obtained from https://doi.org/10.5067/MODIS/MCD12Q1.061 (Friedl et al., 2022). The

https://doi.org/10.5194/egusphere-2026-3708
Preprint. Discussion started: 10 July 2026

MODIS Terra/Aqua Leaf Area Index combined product (MCD15A2H) is available at https://doi.org/10.5067/MODIS/MCD15A2H.061 (Myneni et al., 2021). The Multi-resolution Emission Inventory for China is obtained from http://meicmodel.org.cn/ (Cheng et al., 2023). The Final Analysis dataset is available from https://doi.org/10.5065/D6M043C6 (NCEP, 2000). The monthly BVOC emission inventories generated in this study are publicly available at https://doi.org/10.5281/zenodo.20396128 (Liu et al., 2026)

Author contributions

J. Z., P. F. and H. L. conceived and designed the research. H. L., H. X., Y. S., W. Z., X. Z., and J. D. developed the methodology. H. L. performed the simulations, data analysis and investigation. H. L., Y. H., Y. X., and Q. G. prepared the visualization. The manuscript was primarily written by H. L. and J. Z., with contributions from P. F. All authors discussed the results, commented on the manuscript and gave final approval for publication.

Competing interests

The authors declare that they have no competing interests.

Disclaimer

Publisher's note: Copernicus Publications remains neutral with regard to jurisdictional claims made in the text, published maps, institutional affiliations, or any other geographical representation in this paper. The authors bear the ultimate responsibility for providing appropriate place names. Views expressed in the text are those of the authors and do not necessarily reflect the views of the publisher.

Acknowledgments

We thank the computing resources provided by the National SuperComputer Center in Tianjin, which served as essential research infrastructure for this study. The authors also sincerely thank all colleagues and collaborators who participated in and contributed to this research.

Financial support

This study was supported by the National Natural Science Foundation of China (Grant NO. 42221001)

https://doi.org/10.5194/egusphere-2026-3708
Preprint. Discussion started: 10 July 2026

References

Bai, J., Guenther, A., Turnipseed, A., and Duhl, T.: Seasonal and interannual variations in whole-ecosystem isoprene and monoterpene emissions from a temperate mixed forest in Northern China, Atmospheric Pollution Research, 6, 696-707, https://doi.org/10.5094/APR.2015.078, 2015.

Bai, J., Guenther, A., Turnipseed, A., Duhl, T., Yu, S., and Wang, B.: Seasonal variations in whole-ecosystem BVOC emissions from a subtropical bamboo plantation in China, Atmos. Environ., 124, 12-21, https://doi.org/10.1016/j.atmosenv.2015.11.008, 2016.

Bai, J., Guenther, A., Turnipseed, A., Duhl, T., and Greenberg, J.: Seasonal and interannual variations in whole-ecosystem BVOC emissions from a subtropical plantation in China, Atmos. Environ., 161, 176-190, https://doi.org/10.1016/j.atmosenv.2017.05.002, 2017.

Bai, J., Wu, Z., Yang, C., and Guenther, A.: Seasonal variations in whole-ecosystem BVOC emissions and ozone fluxes from a tropical rubber tree plantation in China, Atmos. Environ., 351, 121182, https://doi.org/10.1016/j.atmosenv.2025.121182, 2025.

Bai, J., Wu, Z., Yang, C., and Guenther, A. B.: Development and application of a generalized empirical model of BVOC emission (GEMBE) using observations from four Chinese forests, Atmospheric Pollution Research, 17, 102814, https://doi.org/10.1016/j.apr.2025.102814, 2026.

Bergman, M. E., Huang, X.-Q., Baudino, S., Caissard, J.-C., and Dudareva, N.: Plant volatile organic compounds: Emission and perception in a changing world, Current Opinion in Plant Biology, 85, 102706, https://doi.org/10.1016/j.pbi.2025.102706, 2025.

Botanic Gardens Conservation International: State of the World's Trees. Botanic Gardens Conservation International, Richmond, UK, 2021.

Cao, H., Fu, T. M., Zhang, L., Henze, D. K., Miller, C. C., Lerot, C., Abad, G. G., De Smedt, I., Zhang, Q., van Roozendael, M., Hendrick, F., Chance, K., Li, J., Zheng, J., and Zhao, Y.: Adjoint inversion of Chinese non-methane volatile organic compound emissions using space-based observations of formaldehyde and glyoxal, Atmos. Chem. Phys., 18, 15017-15046, https://doi.org/10.5194/acp-18-15017-2018, 2018.

Cao, J., Situ, S., Hao, Y., Xie, S., and Li, L.: Enhanced summertime ozone and SOA from biogenic volatile organic compound (BVOC) emissions due to vegetation biomass variability during 1981-2018 in China, Atmos. Chem. Phys., 22, 2351-2364, https://doi.org/10.5194/acp-22-2351-2022, 2022.

Cao, J., Han, H., Qiao, L., and Li, L.: Biogenic Volatile Organic Compound Emission and Its Response to Land Cover Changes in China During 2001-2020 Using an Improved High-Precision Vegetation Data Set, J. Geophys. Res. Atmos., 129, e2023JD040421, https://doi.org/10.1029/2023JD040421, 2024.

Chen, W. H., Guenther, A. B., Wang, X. M., Chen, Y. H., Gu, D. S., Chang, M., Zhou, S. Z., Wu, L. L., and Zhang, Y. Q.: Regional to Global Biogenic Isoprene Emission Responses to Changes in Vegetation From 2000 to 2015, J. Geophys. Res. Atmos., 123, 3757-3771, https://doi.org/10.1002/2017JD027934, 2018.

Chen, Y., Zang, R., Yue, T., Zhang, Y., Wang, X., Li, Y., Li, F., and Chen, Q.: 1:100,0000 forest distribution map of China for 2013-2017. Chinese Academy of Forestry, Beijing, China, [data set], https://doi.org/10.12041/geodata.43370179401687.ver1.db, 2020.

Cheng, J., Tong, D., Liu, Y., Geng, G, N., Davis, J, S., He, K, B., and Zhang, Q.*: A synergistic approach to air pollution control and carbon neutrality in China can avoid millions of premature deaths annually by 2060, One Earth, 6, 978-989, https://doi.org/10.1016/j.oneear.2023.07.007, 2023.

https://doi.org/10.5194/egusphere-2026-3708
Preprint. Discussion started: 10 July 2026

Cheng, K., Yang, H., Chen, Y., Yang, Z., Ren, Y., Zhang, Y., Lin, D., Liu, W., Huang, G., Xu, J., Chen, M., Qi, Z., Xu, G., Tao, S., Guan, H., Ma, Q., Wan, H., Hu, T., Su, Y., Wang, Z., Ma, K., and Guo, Q.: How many trees are there in China?, Science Bulletin, 70, 1076-1079, https://doi.org/10.1016/j.scib.2025.02.001, 2025.

Chytrý, M., Řezníčková, M., Novotný, P., Holubová, D., Preislerová, Z., Attorre, F., Biurrun, I., Blažek, P., Bonari, G., Borovyk, D., Čeplová, N., Danihelka, J., Davydov, D., Dřevojan, P., Fahs, N., Guarino, R., Güler, B., Hennekens, S. M., Hrivnák, R., Kalníková, V., Kalusová, V., Kebert, T., Knollová, I., Knotková, K., Koljanin, D., Kuzemko, A., Loidi, J., Lososová, Z., Marcenò, C., Midolo, G., Milanović, D., Mucina, L., Novák, P., Raab-Straube, E. v., Reczyńska, K., Schaminée, J. H. J., Štěpánková, P., Świerkosz, K., Těšitel, J., Těšitelová, T., Tichý, L., Vynokurov, D., Willner, W., and Axmanová, I.: FloraVeg.EU – An online database of European vegetation, habitats and flora, Applied Vegetation Science, 27, e12798, https://doi.org/10.1111/avsc.12798, 2024.

Copernicus Land Monitoring Service: Fraction of Vegetation Cover 1999-2020 (raster 1 km), global, 10-daily – version 2, European Commission, Joint Research Centre [data set], https://doi.org/10.2909/7d726671-9647-4116-8dc3-cf7470a1a782, 2020.

Dey, B., Sjøgren, T. D., Khare, P., Gkatzelis, G. I., Wu, Y., Vasireddy, S., Schultz, M., Knohl, A., Rinnan, R., Hohaus, T., and Pfannerstill, E. Y.: Multi-stress interaction effects on BVOC emission fingerprints from Oak and Beech: A cross-investigation using Machine Learning and Positive Matrix Factorization, Biogeosciences, 23, 1423-1457, https://doi.org/10.5194/bg-23-1423-2026, 2026.

Ding, X., He, Q. F., Shen, R. Q., Yu, Q. Q., and Wang, X. M.: Spatial distributions of secondary organic aerosols from isoprene, monoterpenes, β-caryophyllene, and aromatics over China during summer, J. Geophys. Res. Atmos., 119, 11,877-811,891, https://doi.org/10.1002/2014JD021748, 2014.

Du, W., Sun, Y., Xu, Y., Jiang, Q., Wang, Q., Yang, W., Wang, F., Bai, Z., Zhao, X., and Yang, Y.: Chemical characterization of submicron aerosol and particle growth events at a national background site (3295 m asl) on the Tibetan Plateau, Atmos. Chem. Phys., 15, 10811-10824, https://doi.org/10.5194/acp-15-10811-2015, 2015.

Emmons, L. K., Walters, S., Hess, P. G., Lamarque, J. F., Pfister, G. G., Fillmore, D., Granier, C., Guenther, A., Kinnison, D., Laepple, T., Orlando, J., Tie, X., Tyndall, G., Wiedinmyer, C., Baughcum, S. L., and Kloster, S.: Description and evaluation of the Model for Ozone and Related chemical Tracers, version 4 (MOZART-4), Geosci. Model Dev., 3, 43-67, https://doi.org/10.5194/gmd-3-43-2010, 2010.

Friedl, M., and Sulla-Menashe, D.: MODIS/Terra+Aqua Land Cover Type Yearly L3 Global 500m SIN Grid V061. NASA Land Processes Distributed Active Archive Center [data set]. https://doi.org/10.5067/MODIS/MCD12Q1.061, 2022.

Fischer, G., F. Nachtergaele, S. Prieler, H.T. van Velthuizen, L. Verelst, D. Wiberg.: Global Agro-ecological Zones Assessment for Agriculture (GAEZ 2008). IIASA, Laxenburg, Austria and FAO, Rome, Italy, 2008

Fu, Y. and Liao, H.: Simulation of the interannual variations of biogenic emissions of volatile organic compounds in China: Impacts on tropospheric ozone and secondary organic aerosol, Atmos. Environ., 59, 170-185, https://doi.org/10.1016/j.atmosenv.2012.05.053, 2012.

Gao, C., Zhang, X., Yang, H., Huang, L., Zhao, H., Zhang, S., and Xiu, A.: Quantifying the impacts of environmental stress factors on biogenic volatile organic compound emissions in China, Agricultural and Forest Meteorology, 366, 110480, https://doi.org/10.1016/j.agrformet.2025.110480, 2025.

https://doi.org/10.5194/egusphere-2026-3708
Preprint. Discussion started: 10 July 2026

Goldstein, A. H. & Galbally, I. E. Known and Unexplored Organic Constituents in the Earth's Atmosphere, Environ. Sci. Technol., 41, 1514-1521, https://doi.org/10.1021/es072476p, 2007.

Grell, G. A. and Freitas, S. R.: A scale and aerosol aware stochastic convective parameterization for weather and air quality modeling, Atmos. Chem. Phys., 14, 5233-5250, https://doi.org/10.5194/acp-14-5233-2014, 2014.

Guenther, A. B., Jiang, X., Heald, C. L., Sakulyanontvittaya, T., Duhl, T., Emmons, L. K., and Wang, X.: The Model of Emissions of Gases and Aerosols from Nature version 2.1 (MEGAN2.1): an extended and updated framework for modeling biogenic emissions, Geosci. Model Dev., 5, 1471-1492, https://doi.org/10.5194/gmd-5-1471-2012, 2012.

Guenther, A., Jiang, X., Shah, T., Huang, L., Kemball-Cook, S., and Yarwood, G.: Model of Emissions of Gases and Aerosol from Nature Version 3 (MEGAN3) for Estimating Biogenic Emissions, Air Pollution Modeling and its Application XXVI, Cham, 187-192, 2020.

Guenther, A. MEGANv3.21.tar.gz emission calculator code. Zenodo [data set]. https://doi.org/10.5281/zenodo.10526206, 2024a.

Guenther, A.: MEGAN 3.2 input files. Zenodo [data set]. https://doi.org/10.5281/zenodo.10939297, 2024b.

Hu, W. W., Hu, M., Yuan, B., Jimenez, J., Tang, Q., Peng, J., Hu, W., Shao, M., Wang, M., and Zeng, L.: Insights on organic aerosol aging and the influence of coal combustion at a regional receptor site of central eastern China, Atmos. Chem. Phys., 13, 10095-10112, https://doi.org/10.5194/acp-13-10095-2013, 2013.

Hu, W., Hu, M., Hu, W.-W., Niu, H., Zheng, J., Wu, Y., Chen, W., Chen, C., Li, L., and Shao, M.: Characterization of submicron aerosols influenced by biomass burning at a site in the Sichuan Basin, southwestern China, Atmos. Chem. Phys., 16, 13213-13230, https://doi.org/10.5194/acp-16-13213-2016, 2016.

Huang, X.-F., He, L.-Y., Hu, M., Canagaratna, M., Kroll, J., Ng, N., Zhang, Y.-H., Lin, Y., Xue, L., and Sun, T.-L.: Characterization of submicron aerosols at a rural site in Pearl River Delta of China using an Aerodyne High-Resolution Aerosol Mass Spectrometer, Atmos. Chem. Phys., 11, 1865-1877, https://doi.org/10.5194/acp-11-1865-2011, 2011.

Huang, X.-F., Xue, L., Tian, X.-D., Shao, W.-W., Sun, T.-L., Gong, Z.-H., Ju, W.-W., Jiang, B., Hu, M., and He, L.-Y.: Highly time-resolved carbonaceous aerosol characterization in Yangtze River Delta of China: Composition, mixing state and secondary formation, Atmos. Environ., 64, 200-207, https://doi.org/10.1016/j.atmosenv.2012.09.059, 2013.

Iacono, M. J., Delamere, J. S., Mlawer, E. J., Shephard, M. W., Clough, S. A., and Collins, W. D.: Radiative forcing by long-lived greenhouse gases: Calculations with the AER radiative transfer models, J. Geophys. Res. Atmos., 113, https://doi.org/10.1029/2008JD009944, 2008.

Jing, X., Lun, X., Fan, C., and Ma, W.: Emission patterns of biogenic volatile organic compounds from dominant forest species in Beijing, China, J. Environ. Sci., 95, 73-81, https://doi.org/10.1016/j.jes.2020.03.049, 2020.

Kenseth, C. M., Hafeman, N. J., Rezgui, S. P., Chen, J., Huang, Y., Dalleska, N. F., Kjaergaard, H. G., Stoltz, B. M., Seinfeld, J. H., and Wennberg, P. O.: Particle-phase accretion forms dimer esters in pinene secondary organic aerosol, Science, 382, 787-792, https://doi.org/10.1126/science.adi0857, 2023.

Li, L. Y., Chen, Y., and Xie, S. D.: Spatio-temporal variation of biogenic volatile organic compounds emissions in China, Environ. Pollut., 182, 157-168, https://doi.org/10.1016/j.envpol.2013.06.042, 2013.

Li, L. Y. and Xie, S. D.: Historical variations of biogenic volatile organic compound emission inventories in China, 1981-2003, Atmos. Environ., 95, 185-196, https://doi.org/10.1016/j.atmosenv.2014.06.033, 2014.

Li, J., Liu, Z., Cao, L., Gao, W., Yan, Y., Mao, J., Zhang, X., He, L., Xin, J., and Tang, G.: Highly time-resolved chemical characterization and implications of regional transport for submicron aerosols in the North China Plain, Sci. Total. Environ., 705, 135803, https://doi.org/10.1016/j.scitotenv.2019.135803, 2020a.

https://doi.org/10.5194/egusphere-2026-3708
Preprint. Discussion started: 10 July 2026

Li, L., Yang, W., Xie, S., and Wu, Y.: Estimations and uncertainty of biogenic volatile organic compound emission inventory in China for 2008-2018, Sci. Total. Environ., 733, 139301, https://doi.org/10.1016/j.scitotenv.2020.139301, 2020b.

Li, L., Zhang, B., Cao, J., Xie, S., and Wu, Y.: Isoprenoid emissions from natural vegetation increased rapidly in eastern China, Environmental Research, 200, 111462, https://doi.org/10.1016/j.envres.2021.111462, 2021.

Li, L., Cao, J., and Hao, Y.: Spatial and species-specific responses of biogenic volatile organic compound (BVOC) emissions to elevated ozone from 2014-2020 in China, Sci. Total. Environ., 868, 161636, https://doi.org/10.1016/j.scitotenv.2023.161636, 2023.

Li, Q., Lerner, G., Bar, E., Lewinsohn, E., and Tas, E.: Impact of meteorological conditions on the biogenic volatile organic compound (BVOC) emission rate from eastern Mediterranean vegetation under drought, Biogeosciences, 21, 4133-4147, https://doi.org/10.5194/bg-21-4133-2024, 2024.

Li, P., Yu, Y., and Zhao, S.: Comparative assessment of MEGAN v2.1 and v3.2 biogenic VOC emissions over the Qinghai-Tibet Plateau: implications for summertime surface ozone simulations, EGUsphere, 2025, 1-30, https://doi.org/10.5194/egusphere-2025-5579, 2025.

Liu, S., Xing, J., Zhang, H., Ding, D., Zhang, F., Zhao, B., Sahu, S. K., and Wang, S.: Climate-driven trends of biogenic volatile organic compound emissions and their impacts on summertime ozone and secondary organic aerosol in China in the 2050s, Atmos. Environ., 218, 117020, https://doi.org/10.1016/j.atmosenv.2019.117020, 2019.

Liu, H., Xu, H., Huang, Y., Zhou, W., Xiao, Y., Guo, Q., Zhao, X., Deng, J., Sun, Y., Fu, P., and Zhu, J.: Species-explicit modelling of forest biogenic volatile organic emissions across China, Zenodo [data set], https://doi.org/10.5281/zenodo.20396128, 2026.

Ma, J., Zhu, S., Wang, S., Wang, P., Chen, J., and Zhang, H.: Impacts of land cover changes on biogenic emission and its contribution to ozone and secondary organic aerosol in China, Atmos. Chem. Phys., 23, 4311-4325, https://doi.org/10.5194/acp-23-4311-2023, 2023.

Mallapaty, S.: How China could be carbon neutral by mid-century, Nature, 586, 482-483, https://doi.org/10.1038/d41586-020-02927-9, 2020.

Morrison, H., Thompson, G., and Tatarskii, V.: Impact of Cloud Microphysics on the Development of Trailing Stratiform Precipitation in a Simulated Squall Line: Comparison of One- and Two-Moment Schemes, Monthly Weather Review, 137, 991-1007, https://doi.org/10.1175/2008MWR2556.1, 2009.

Myneni, R., Knyazikhin, Y., and Park, T.: MODIS/Terra+Aqua Leaf Area Index/FPAR 8-Day L4 Global 500m SIN Grid V061, NASA EOSDIS Land Processes Distributed Active Archive Center [data set], https://doi.org/10.5067/MODIS/MCD15A2H.061, 2021.

Nakanishi, M. and Niino, H.: An Improved Mellor-Yamada Level-3 Model: Its Numerical Stability and Application to a Regional Prediction of Advection Fog, Boundary-Layer Meteorology, 119, 397-407, https://doi.org/10.1007/s10546-005-9030-8, 2006.

National Centers for Environmental Prediction/National Weather Service/NOAA/U.S. Department of Commerce: NCEP FNL Operational Model Global Tropospheric Analyses, continuing from July 1999, NSF National Center for Atmospheric Research [data set], https://doi.org/10.5065/D6M043C6, 2000.

Niinemets, Ü. and Reichstein, M.: Controls on the emission of plant volatiles through stomata: Differential sensitivity of emission rates to stomatal closure explained, J. Geophys. Res. Atmos., 108, https://doi.org/10.1029/2002JD002620, 2003.

https://doi.org/10.5194/egusphere-2026-3708
Preprint. Discussion started: 10 July 2026

Nowak, David J.: Understanding i-Tree: 2023 summary of programs andmethods, U.S. Department of Agriculture, Forest Service, Northern Research Station, USA, https://doi.org/10.2737/NRS-GTR-200-2023, 2024.

Oleson, K. W., Lawrence, D. M., Bonan, G. B., Fisher, R. A., Lawrence, P. J., & Muszala, S. P.: Technical description of version 4.5 of the Community Land Model (CLM), NCAR/TN-503+ STR, 503, 2013.

Opacka, B., Müller, J. F., Stavrakou, T., Bauwens, M., Sindelarova, K., Markova, J., and Guenther, A. B.: Global and regional impacts of land cover changes on isoprene emissions derived from spaceborne data and the MEGAN model, Atmos. Chem. Phys., 21, 8413-8436, https://doi.org/10.5194/acp-21-8413-2021, 2021.

Pöschl, U., Martin, S. T., Sinha, B., Chen, Q., Gunthe, S. S., Huffman, J. A., Borrmann, S., Farmer, D. K., Garland, R. M., Helas, G., Jimenez, J. L., King, S. M., Manzi, A., Mikhailov, E., Pauliquevis, T., Petters, M. D., Prenni, A. J., Roldin, P., Rose, D., Schneider, J., Su, H., Zorn, S. R., Artaxo, P., and Andreae, M. O.: Rainforest Aerosols as Biogenic Nuclei of Clouds and Precipitation in the Amazon, Science, 329, 1513-1516, https://doi.org/10.1126/science.1191056, 2010.

Qin, Y. M., Tan, H. B., Li, Y. J., Schurman, M. I., Li, F., Canonaco, F., Prévôt, A. S., and Chan, C. K.: Impacts of traffic emissions on atmospheric particulate nitrate and organics at a downwind site on the periphery of Guangzhou, China, Atmos. Chem. Phys., 17, 10245-10258, https://doi.org/10.5194/acp-17-10245-2017, 2017.

Rissanen, K., Aalto, J., Bäck, J., Hellén, H., Tykkä, T., and Paquette, A.: Variability in BVOC emissions a nd air quality impacts among urban trees in Montreal and Helsinki, Atmos. Chem. Phys., 25, 15415-15435, https://doi.org/10.5194/acp-25-15415-2025, 2025.

Sahu, A., Mostofa, M. G., Weraduwage, S. M., and Sharkey, T. D.: Hydroxymethylbutenyl diphosphate accumulation reveals MEP pathway regulation for high CO2-induced suppression of isoprene emission, Proc. Natl Acad. Sci. USA, 120, e2309536120, https://doi.org/10.1073/pnas.2309536120, 2023.

Sanaei, A., Herrmann, H., Alshaabi, L., Beck, J., Ferlian, O., Fomba, K. W., Haferkorn, S., van Pinxteren, M., Quaas, J., Quosh, J., Rabe, R., Wirth, C., Eisenhauer, N., and Weigelt, A.: Changes in biodiversity impact atmospheric chemistry and climate through plant volatiles and particles, Commun. Earth Environ., 4, 445, https://doi.org/10.1038/s43247-023-01113-9, 2023.

Skamarock, W. C., Klemp, J. B., Dudhia, J., Gill, D. O., Liu, Z., Berner, J., Wang, W., Powers, J. G., Duda, M. G., and Barker, D. M.: A description of the advanced research WRF version 4, NCAR tech. note ncar/tn-556+str, 145, 2019.

State Forestry and Grassland Administration of the People's Republic of China: National Forest Management Plan (2016-2050) (in Chinese), State Forestry and Grassland Administration of the People's Republic of China, Beijing, China, http://official.csf.org.cn/AttachFile/2016/1010020506/0/636076549549475902.pdf, 2016.

State Forestry and Grassland Administration of the People's Republic of China: Ninth National Forest Resource Inventory Report (2014-2018) (in Chinese), State Forestry and Grassland Administration of the People's Republic of China, Beijing, China, https://doi.org/10.12459.11.0120020909213.0001.V1, 2020.

State Forestry and Grassland Administration of the People's Republic of China: China's Forest Genetic Resources Country Report (in Chinese), State Forestry and Grassland Administration of the People's Republic of China, Beijing, China, https://www.fao.org/4/i3825e/i3825e13a.pdf, 2022.

Stavrakou, T., Müller, J. F., Bauwens, M., De Smedt, I., Van Roozendael, M., Guenther, A., Wild, M., and Xia, X.: Isoprene emissions over Asia 1979–2012: impact of climate and land-use changes, Atmos. Chem. Phys., 14, 4587-4605, https://doi.org/10.5194/acp-14-4587-2014, 2014.

https://doi.org/10.5194/egusphere-2026-3708
Preprint. Discussion started: 10 July 2026

Stenke, A.: Natural control on ozone pollution, Nat. Clim. Change, 10, 101-102, 10.1038/s41558-019-0686-3, 2020.

Tian, X., Zeng, J., Zhang, Y., Pang, W., Lu, Y., Ran, H., Guo, H., Mu, Z., Song, W., and Wang, X.: Measurement report: Age-dependent BVOC emissions in Eucalyptus urophylla: a comparison of leaf cuvette and branch chamber measurements, Atmos. Chem. Phys., 26, 6213-6221, https://doi.org/10.5194/acp-26-6213-2026, 2026.

Vella, R., Forrest, M., Pozzer, A., Tsimpidi, A. P., Hickler, T., Lelieveld, J., and Tost, H.: Influence of land cover change on atmospheric organic gases, aerosols, and radiative effects, Atmos. Chem. Phys., 25, 243-262, https://doi.org/10.5194/acp-25-243-2025, 2025.

Wang, X., Situ, S., Chen, W., Zheng, J., Guenther, A., Fan, Q., and Chang, M.: Numerical model to quantify biogenic volatile organic compound emissions: The Pearl River Delta region as a case study, J Environ Sci (China), 46, 72-82, https://doi.org/10.1016/j.jes.2015.08.032, 2016a.

Wang, Q., Zhao, J., Du, W., Ana, G., Wang, Z., Sun, L., Wang, Y., Zhang, F., Li, Z., and Ye, X.: Characterization of submicron aerosols at a suburban site in central China, Atmos. Environ., 131, 115-123, https://doi.org/10.1016/j.atmosenv.2016.01.054, 2016b.

Wang, H., Wu, Q., Guenther, A. B., Yang, X., Wang, L., Xiao, T., Li, J., Feng, J., Xu, Q., and Cheng, H.: A long-term estimation of biogenic volatile organic compound (BVOC) emission in China from 2001-2016: the roles of land cover change and climate variability, Atmos. Chem. Phys., 21, 4825-4848, https://doi.org/10.5194/acp-21-4825-2021, 2021.

Wang, H., Lu, X., Seco, R., Stavrakou, T., Karl, T., Jiang, X., Gu, L., and Guenther, A. B.: Modeling Isoprene Emission Response to Drought and Heatwaves Within MEGAN Using Evapotranspiration Data and by Coupling With the Community Land Model, Journal of Advances in Modeling Earth Systems, 14, e2022MS003174, https://doi.org/10.1029/2022MS003174, 2022.

Wang, H., Liu, X., Wu, C., and Lin, G.: Regional to global distributions, trends, and drivers of biogenic volatile organic compound emission from 2001 to 2020, Atmos. Chem. Phys., 24, 3309-3328, https://doi.org/10.5194/acp-24-3309-2024, 2024a.

Wang, H., Welch, A. M., Nagalingam, S., Leong, C., Czimczik, C. I., Tang, J., Seco, R., Rinnan, R., Vettikkat, L., Schobesberger, S., Holst, T., Brijesh, S., Sheesley, R. J., Barsanti, K. C., and Guenther, A. B.: High temperature sensitivity of Arctic isoprene emissions explained by sedges, Nat. Commun., 15, 6144, https://doi.org/10.1038/s41467-024-49960-0, 2024b.

Wang, N., Liu, S., Xu, J., Wang, Y., Li, C., Xie, Y., Lu, H., and Yang, F.: Climate-driven biogenic emissions alleviate the impact of human-made emission reductions on O3 control in the Pearl River Delta region, southern China, Atmos. Chem. Phys., 25, 8859-8870, https://doi.org/10.5194/acp-25-8859-2025, 2025.

Wu, Z.: Forest in China Vol. 1, China Forestry Publishing House, Beijing. China, 1997.

Wu, K., Yang, X., Chen, D., Gu, S., Lu, Y., Jiang, Q., Wang, K., Ou, Y., Qian, Y., Shao, P., and Lu, S.: Estimation of biogenic VOC emissions and their corresponding impact on ozone and secondary organic aerosol formation in China, Atmos. Res., 231, 104656, https://doi.org/10.1016/j.atmosres.2019.104656, 2020.

Wu, J., Zhang, Q., Wang, L., Li, L., Lun, X., Chen, W., Gao, Y., Huang, L., Wang, Q., and Liu, B.: Seasonal biogenic volatile organic compound emission factors in temperate tree species: Implications for emission estimation and ozone formation, Environ. Pollut., 361, 124895, https://doi.org/10.1016/j.envpol.2024.124895, 2024.

Xi, S., Wang, Y., Yuan, X., Feng, Z., Zhao, F., Zhang, Y., and Wang, X.: The Speciated isoprene emission model with the MEGAN algorithm for China (SieMAC), Geosci. Model Dev., 18, 8627-8649, 10.5194/gmd-18-8627-2025, 2025.

Xu, J., Zhang, Q., Shi, J., Ge, X., Xie, C., Wang, J., Kang, S., Zhang, R., and Wang, Y.: Chemical characteristics of

https://doi.org/10.5194/egusphere-2026-3708
Preprint. Discussion started: 10 July 2026

submicron particles at the central Tibetan Plateau: insights from aerosol mass spectrometry, Atmos. Chem. Phys., 18, 427-443, https://doi.org/10.5194/acp-18-427-2018, 2018.

Xu, H., Yue, C., Zhang, Y., Liu, D., and Piao, S.: Forestation at the right time with the right species can generate persistent carbon benefits in China, Proc. Natl Acad. Sci. USA, 120, e2304988120, 10.1073/pnas.2304988120, 2023a.

Hao Xu.: Forestation at the right time with the right species can generate persistent carbon benefits in China, Zenodo [data set]. https://doi.org/10.5281/zenodo.8297679, 2023b.

Xu, J., Silver, B., Tang, R., Wang, N., Huang, X., Ding, A., and Arnold, S. R.: A model assessment of the relationship between urban greening and ozone air quality in China: a study of three metropolitan regions, npj Clim. Atmos. Sci., 8, 184, https://doi.org/10.1038/s41612-025-01054-4, 2025.

Yu, H., Buchholz, A., Pullinen, I., Saarela, S., Li, Z., Virtanen, A., and Blande, J. D.: Biogenic secondary organic aerosol participates in plant interactions and herbivory defense, Science, 385, 1225-1230, https://doi.org/10.1126/science.ado6779, 2024.

Zaveri, R. A., Easter, R. C., Fast, J. D., and Peters, L. K.: Model for Simulating Aerosol Interactions and Chemistry (MOSAIC), J. Geophys. Res. Atmos., 113, https://doi.org/10.1029/2007JD008782, 2008.

Zheng, J., Hu, M., Du, Z., Shang, D., Gong, Z., Qin, Y., Fang, J., Gu, F., Li, M., and Peng, J.: Influence of biomass burning from South Asia at a high-altitude mountain receptor site in China, Atmos. Chem. Phys., 17, 6853-6864, https://doi.org/10.5194/acp-17-6853-2017, 2017.

Zhang, Y., Du, W., Wang, Y., Wang, Q., Wang, H., Zheng, H., Zhang, F., Shi, H., Bian, Y., and Han, Y.: Aerosol chemistry and particle growth events at an urban downwind site in North China Plain, Atmos. Chem. Phys., 18, 14637-14651, https://doi.org/10.5194/acp-18-14637-2018, 2018a.

Zhang, X., Xu, J., Kang, S., Liu, Y., and Zhang, Q.: Chemical characterization of long-range transport biomass burning emissions to the Himalayas: insights from high-resolution aerosol mass spectrometry, Atmos. Chem. Phys., 18, 4617-4638, https://doi.org/10.5194/acp-18-4617-2018, 2018b.

Zhang, X., Xu, J., Kang, S., Zhang, Q., and Sun, J.: Chemical characterization and sources of submicron aerosols in the northeastern Qinghai-Tibet Plateau: insights from high-resolution mass spectrometry, Atmos. Chem. Phys., 19, 7897-7911, https://doi.org/10.5194/acp-19-7897-2019, 2019.

Zhang, Z., Xu, W., Zhang, Y., Zhou, W., Xu, X., Du, A., Zhang, Y., Qiao, H., Kuang, Y., and Pan, X.: Measurement report: Impact of cloud processes on secondary organic aerosols at a forested mountain site in southeastern China, Atmos. Chem. Phys., 24, 8473-8488, https://doi.org/10.5194/acp-24-8473-2024, 2024.

Zhang, C., Bäck, J., Peñuelas, J., Liu, D., Filella, I., Porcar-Castell, A., and Atherton, J.: Connecting optical remote sensing of plant photosynthesis with biogenic volatile organic compound emissions, New Phytologist, 248, 494-506, https://doi.org/10.1111/nph.70504, 2025.

Zhu, Q., He, L.-Y., Huang, X.-F., Cao, L.-M., Gong, Z.-H., Wang, C., Zhuang, X., and Hu, M.: Atmospheric aerosol compositions and sources at two national background sites in northern and southern China, Atmos. Chem. Phys., 16, 10283-10297, https://doi.org/10.5194/acp-16-10283-2016, 2016.

Zhu, J., Penner, J. E., Hong, C., Liu, H., Zhao, X., Deng, J., Liu, C.-Q., Zhang, Q., and Fu, P.: Cropland expansion reduces biogenic secondary organic aerosol and associated radiative cooling, Nat. Geosci., 18, 624-630, https://doi.org/10.1038/s41561-025-01718-z, 2025.